Appendices

Appendix I P. Hapala et al., *Phys. Rev. B* **90**, 085421 (2014).
Appendix II P. Hapala et al., *Phys. Rev. Lett.* **113**, 226101 (2014).
Appendix III F. Albrecht et al., *Phys. Rev. Lett.* **115**, 076101 (2015).
Appendix IV M. Corso et al., *Phys. Rev. Lett.* **115**, 136101 (2015).
Appendix V K. Iwata et al., *Nat. Commun.* **6**, 7766 (2015).
Appendix VI J. Berger et al., *J. Phys. Chem. C* **120**, 21955 (2016).
Appendix VII N. J. van der Heijden et al., *ACS Nano* **10**, 8517 (2016).
Appendix VIII J. van der Lit et al., *Phys. Rev. Lett.* **116**, 096102 (2016).
Appendix IX P. Hapala et al., *Nat. Commun.* **7**, 11560 (2016).
Appendix X N. Kocić et al., *J. Am. Chem. Soc.* **138**, 5585 (2016).
Appendix XI O. Stetsovych et al., *Nat. Chem.* **9**, 213 (2017).
Appendix XII O. Krejčí et al., *Phys. Rev. B* **95**, 045407 (2017).

PHYSICAL REVIEW B **90**, 085421 (2014)

Mechanism of high-resolution STM/AFM imaging with functionalized tips

Prokop Hapala[*]
Institute of Physics, Academy of Sciences of the Czech Republic, v.v.i., Cukrovarnická 10, 162 00 Prague, Czech Republic

Georgy Kichin, Christian Wagner, F. Stefan Tautz, and Ruslan Temirov[†]
Peter Grünberg Institut (PGI-3), Forschungszentrum Jülich, 52425 Jülich, Germany
and Jülich Aachen Research Alliance (JARA), Fundamentals of Future Information Technology, 52425 Jülich, Germany

Pavel Jelínek[‡]
Institute of Physics, Academy of Sciences of the Czech Republic, v.v.i., Cukrovarnická 10, 162 00 Prague, Czech Republic
and Graduate School of Engineering, Osaka University 2-1, Yamada-Oka, Suita, Osaka 565-0871, Japan

(Received 16 June 2014; revised manuscript received 23 July 2014; published 19 August 2014)

High-resolution atomic force microscopy (AFM) and scanning tunneling microscopy (STM) imaging with functionalized tips is well established, but a detailed understanding of the imaging mechanism is still missing. We present a numerical STM/AFM model, which takes into account the relaxation of the probe due to the tip-sample interaction. We demonstrate that the model is able to reproduce very well not only the experimental intra- and intermolecular contrasts, but also their evolution upon tip approach. At close distances, the simulations unveil a significant probe particle relaxation towards local minima of the interaction potential. This effect is responsible for the sharp submolecular resolution observed in AFM/STM experiments. In addition, we demonstrate that sharp apparent intermolecular bonds should not be interpreted as true hydrogen bonds, in the sense of representing areas of increased electron density. Instead, they represent the ridge between two minima of the potential energy landscape due to neighboring atoms.

DOI: 10.1103/PhysRevB.90.085421 PACS number(s): 68.37.Ef, 68.37.Ps, 82.30.Rs, 68.49.Df

I. INTRODUCTION

Scanning tunneling microscopy (STM) [1] and atomic force microscopy (AFM) [2] methods are key tools of nanoscience. One of their most remarkable achievement is the unprecedented submolecular resolution of both atomic and electronic structures of single molecules on surfaces. First real space images of molecular orbitals were obtained with STM [3]. Then it was found that functionalizing the tip with a single carbon monoxide (CO) molecule enhances the resolution of molecular orbital STM images [4,5]. Later it has been discovered that STM tip functionalization with H_2, D_2 [so-called scanning tunneling hydrogen microscopy (STHM) [6,7]] and a variety of other atomic and molecular particles (Xe, CH_4, CO) allows the STM to resolve the *atomic* structures of large organic adsorbates in a direct imaging experiment [6–9]. Finally, the development of the qPlus AFM technique [10] has resulted in the successful resolution of internal molecular structures by AFM [11,12].

On the basis of a density functional theory (DFT) analysis the high resolution of molecular structures in AFM has been attributed to Pauli repulsion [11,13]. Following this result it has been proposed that the contrast delivered by functionalized STM tips is related to the same force [7]. Several groups have also pointed out the influence of CO-tip bending on the distortion that is present in high-resolution AFM images [12,14,15].

One peculiar feature of the high-resolution STM/AFM images obtained with functionalized tips, namely the striking imaging contrast obtained in areas between molecules [8,9,16,17], has, however, not yet been clearly explained. In particular, the sharp ridges observed in the high-resolution images do not necessarily represent a true bond. For example, Pavlicek *et al.* [18] observed in high-resolution images of DBTH molecules an apparent bond ridge between sulfur atoms where there is no chemical bond.

Very recently it has been argued that sharp contrast features between the molecules may be related to the imaging of hydrogen bonds [17], as a consequence of an enhanced electron density between oxygen and hydrogen atoms of neighboring molecules. But it is not clear why in experiment this contrast appears so sharp, especially since according to DFT simulations the electron density variation is expected to be exceedingly small [17]. The sharp lines visible in these experiments therefore cannot be automatically ascribed to (hydrogen) bonds. This calls for a deeper understanding of the origin of the high-resolution contrast in general.

In this work we propose a simple mechanical model of the functionalized STM/AFM junction that clarifies all of the main features of STM and AFM images measured with functionalized tips. First, it explains the appearance of characteristic sharp features in STM and AFM images measured at close tip-sample distances. Secondly, it establishes the relationship between the observed AFM and STM image contrasts obtained with functionalized tips. Thirdly, it reveals the nature of the STM and AFM contrasts in the intermolecular regions and allows a critical discussion of the appearance of so-called hydrogen bonds in the images. Finally, the method allows us to simulate AFM/STM images of complete molecular layers at different tip-sample distances at small

---

[*] Corresponding author: hapala@fzu.cz
[†] r.temirov@fz-juelich.de
[‡] pavel.jelinek@fzu.cz

computational cost. To underpin the predictive power of our model, we compare AFM/STM images obtained from our numerical model to selected experimental cases.

II. METHODS

A. Equipment and sample preparation

The experiments were performed using a combined NC-AFM/STM from Createc. The base pressure at the working temperature of 5 K was better than 10^{-11} mbar. All samples were prepared using standard techniques of surface preparation in ultrahigh vacuum. Submonolayer coverages of PTCDA were deposited onto freshly prepared surfaces of Au(111) and Ag(111) at room temperature using a homebuilt Knudsen cell. Immediately after the deposition the sample was transferred to the cold (5 K) STM. Individual xenon atoms and carbon monoxide molecules were deposited onto the sample at 5 K by closing the ion getter pump, opening the shutter in the cryoshields, and flooding the STM chamber with the clean gas for 10 min at a pressure of about 5×10^{-9} mbar. The tip decoration was effected according to the procedures described in Ref. [8].

B. Preparation molecular geometry for simulation

The molecular geometry of PTCDA monolayers on the respective metallic substrates was determined from supercell parameters obtained from Ref. [19] in the case of Au(111) and from Ref. [20] for Ag(110). Atomic coordinates for the 8-hydroxyquinoline tetramer were taken from Ref. [17]. The molecular geometries were then relaxed in the relevant supercell using the local orbital DFT code FIREBALL [21,22] within the local-density approximation (LDA) for the exchange-correlation functional. During the relaxation the molecular geometry was free to move in the x,y plane, while the z coordinates of all atoms were set to $z = 0$ and fixed. Convergence was achieved once a residual total energy of 0.0001 eV and a maximal force of 0.05 eV/Å were reached. The atomic structure of NTCDI molecules on Ag:Si(111)-($\sqrt{3}\times\sqrt{3}$) was taken from DFT calculations published in Ref. [23] (see Fig. 3.C of that reference).

C. Mechanical AFM model

The main ingredient of our model is the geometric distortion of the "soft" apex of a functionalized tip due to the interaction with the surface [12]. We model this soft apex as the outermost atom of the metal tip (*tip base*) and the *probe particle* that decorates it (see Fig. 1).

To account for the interaction between the functionalized tip and a molecular layer ("sample") on the surface we construct a force-field model of the junction using empirical potentials. In particular, we use a pairwise Lennard-Jones (LJ) potential to describe the weak interaction F_{Surf} between the probe particle of the functionalized tip and the sample (see Fig. 1). F_{Surf} is calculated as a sum of all pairwise LJ forces acting between the probe particle and the atoms constituting the molecular layer. Besides F_{Surf} the probe particle experiences two additional forces: (i) a radial LJ force $F_{\mathrm{Tip,R}}$ between the probe particle and the tip base which keeps the probe particle attached to the tip base at a particular distance and (ii) an additional lateral harmonic force $F_{\mathrm{Tip,xy}}$ that stems from the cylindrically symmetric attractive potential of the tip base.

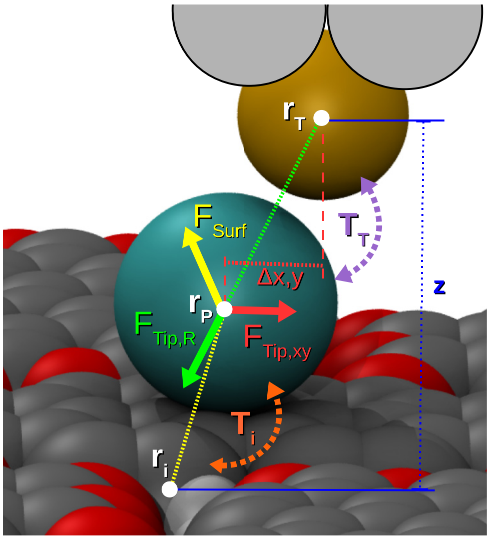

FIG. 1. (Color online) AFM/STM model. Schematic view of the mechanical model of a functionalized tip as employed in this work. The last metal atom of the tip (*tip base*) is shown in sand color, the probe particle in cyan, and the molecular layer (*sample*, in the example a herringbone PTCDA layer) in gray (carbon atoms) and red (oxygen atoms). The forces acting on the probe particle are shown in color: radial tip force $F_{\mathrm{Tip,R}}$ (green); lateral tip force $F_{\mathrm{Tip,xy}}$ (red); force F_{Surf} exerted by atoms of the sample (yellow). Force-determining geometric parameters are shown in the same color as the corresponding forces. The two distinct hopping processes in our STM model are denoted by violet (probe particle tip, T_T) and orange (probe particle sample, T_i) color. The reference distance z that is used throughout the paper is shown in blue.

In this work we employ two different sets of LJ parameters (binding energy ϵ_α and equilibrium distance r_α) of the $F_{\mathrm{Tip,R}}$ interaction to mimic Xe- and CO-decorated tips (cf. Supplemental Material [25], Table 1), while the lateral stiffness $k_{xy} = 0.5$ N/m is kept constant for all types of probe particles. Interestingly, we find that the results depend only weakly on variations of the binding energy parameter ϵ_α (cf. Supplemental Material [25], Fig. 1). This observation agrees well with the fact that the high-resolution images of a particular molecule obtained with different functionalized tips look qualitatively similar [26]. It turns out that the variation of the image contrast between different probe particles is mainly related to their different van der Waals radii, in our model defined by r_α (cf. Supplemental Material [25], Fig. 2). The Lennard-Jones parameters used in the mechanical model of probe particle relaxation for H, C, O, and Xe atoms were taken from the OPLS force field [24] (for more details, see Supplemental Material [25], Table 1 and methods). The robustness of the simulations with respect to the precise values of these parameters is demonstrated in the Supplemental Material [25], Figs. 1–3. Regarding the procedure with which the simulated AFM images were generated, refer to methods in Supplemental Material [25].

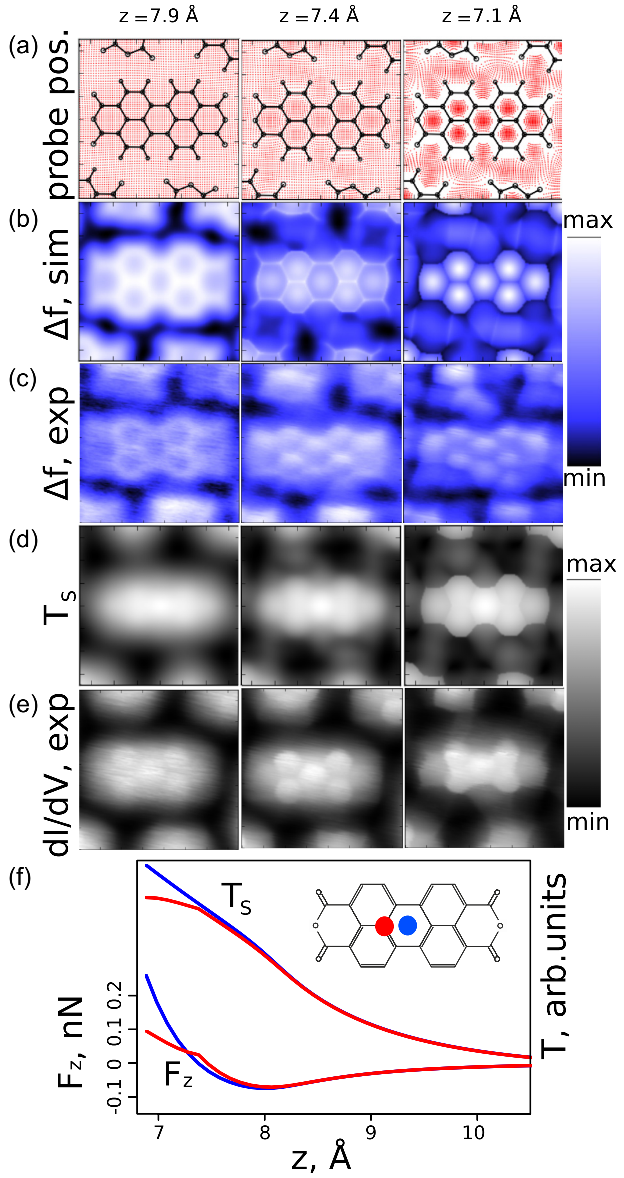

FIG. 2. (Color online) Simulated and experimental high-resolution AFM and STM images. Experimental images have been recorded on PTCDA/Au(111) with a CO probe particle. Simulated images have been obtained with LJ parameters mimicking the oxygen atom of CO. (a) Map of simulated probe particle positions after relaxation. (b) Simulated AFM image (the frequency shift Δf is displayed). (c) Experimental AFM images (frequency shift). (d) Simulated STM images (maps of the T_S tunneling process). (e) Experimental STM images (differential conductance). (f) Vertical force F_z (left axis) and tunneling probability T_S (right axis, arbitrary units), both as a function of tip-sample distance z, computed over different sites of the sample as indicated by the red and blue dots in the PTCDA structure formula. Experimental images in panels (c) and (e) are taken from Ref. [9]). All simulated images except (a) are normalized to obtain maximum contrast.

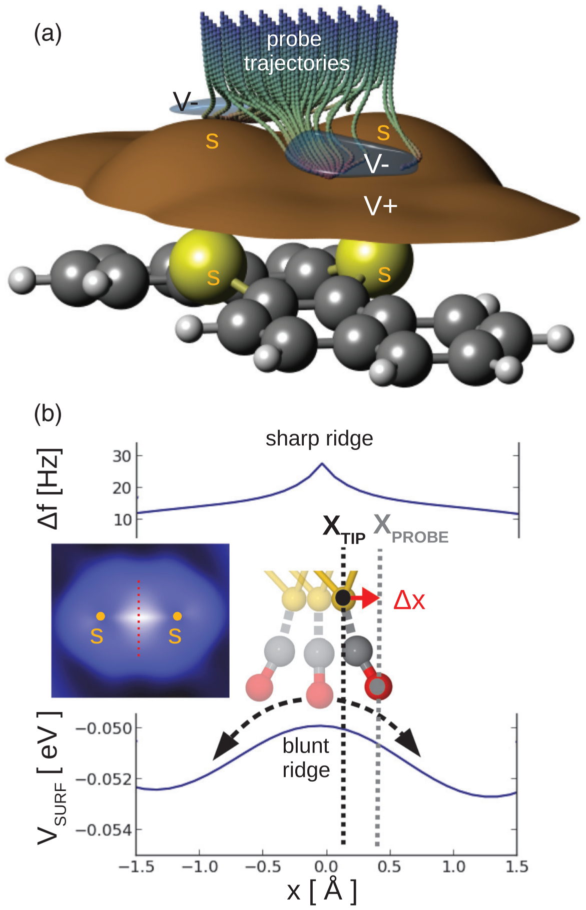

FIG. 3. (Color online) Origin of sharp lines in AFM images. (a) DBTH molecule (sulfur atoms in yellow, carbon atoms in dark gray, and hydrogen atoms in light gray), with repulsive potential felt by the probe particle in brown ($V+$) and attractive basins ($V-$) in blue. Probe particle trajectories upon tip approach are also shown. Sulfur-derived hillocks in the repulsive potential are labeled "S." Between them, a repulsive saddle is formed. (b) Surface potential V^{Surf} (bottom) and AFM frequency shift Δf (top) along the central cross section of the repulsive saddle. In the center the relaxation Δx of the probe particle towards the position x_{probe} is shown schematically for a tip position x_{tip} close to the ridge of the saddle. The mapping of the force at x_{probe} to the macroscopic tip position x_{tip} explains the sharpening of the Δf curve ("sharp ridge") even for a smooth saddle in V^{Surf} ("blunt ridge"). The inset shows a simulated AFM image of DBTH in the region of the two sulfur atom, clearly exhibiting the sharp line between the two sulfur atoms.

We use our model to simulate the images of the well-known herringbone monolayer of 3,4,9,10-perylene tetracarboxylic dianhydride (PTCDA). PTCDA layers, as well as single PTCDA molecules, have been extensively imaged with functionalized STM/AFM tips [6–9,16,27]. Therefore, a wealth of experimental data is readily available for direct comparison to the results of our simulations. As mentioned above, the input atomic structure of the molecular layer was taken from the data published for PTCDA/Au(111) [19], and the structure was further optimized with DFT.

The simulated data were acquired by scanning the model tip laterally over the surface with a step of $\Delta x, \Delta y = 0.1$ Å. At each lateral position, the tip was placed at an initial set point $z_0 = 12$ Å above the molecular layer (cf. Fig. 1 for the definition of the z coordinate). Subsequently, we approached the tip vertically towards the sample in steps of $\Delta z = 0.1$ Å until $z = 6$ Å. At each step of the vertical approach the probe particle position was allowed to relax until the net force

$F_{\mathrm{Surf}} + F_{\mathrm{Tip,R}} + F_{\mathrm{Tip,xy}}$ acting on the probe particle (see Fig. 1) became smaller than 10^{-6} eV/Å. At the same time the degrees of freedom of the molecular layer and the tip base were kept fixed. Once the structural relaxation was completed, the vertical force F_z was calculated from a projection of F_{Surf} onto the z axis. Finally, the $F_z(z)$ curves were converted to frequency shift $\Delta f(z)$ using the inverse Sader formula [28].We note that in our experiments the qPlus sensor was oscillating with a very small amplitude (0.2 Å from zero to peak). The same value was used in our numerical simulations.

D. STM model

On top of the mechanical AFM model we derive a simple numerical model for STM simulations, the main objective of which is to understand the variation of the tunneling current as a function of probe particle relaxation. The model is based on Landauer theory [29]. We start from the Landauer formula for the conductance $dI/dV(\epsilon) = \frac{2e}{h}\Gamma_T(\epsilon){G_P}^{\dagger}(\epsilon)\Gamma_S(\epsilon)G_P(\epsilon)$, where $G_P(\epsilon)$ is the Green's function of the probe particle at energy ϵ and $\Gamma_{T,S}(\epsilon) = 2\,\mathrm{Im}\Sigma_{T,S}(\epsilon)$, where the $\Sigma_{T,S}(\epsilon) = {t_{T,S}}^{\dagger}G_{T,S}t_{T,S}$ represent the self-energies of tip (T) and sample (S), respectively; the $t_{T,S}$ quantify the hopping between the probe particle and tip or sample, respectively. To simplify our model we adopt several approximations. (i) We are interested just in the conductance at zero bias voltage, so we set $\epsilon = \epsilon_F$, where ϵ_F is the Fermi energy. (ii) We neglect the real part of the probe particle Green's function, i.e., $\mathrm{Re}G_P(\epsilon_F) \approx 0$, and we express the local density of states (LDOS) of the probe particle as $\rho_P(\epsilon_F) = \frac{1}{\pi}\mathrm{Im}G_P(\epsilon_F)$. In a similar way, we can also rewrite $\Gamma_{T,S}(\epsilon_F) \approx {t_{T,S}}^{\dagger}(\epsilon_F)\rho_{T,S}(\epsilon_F)t_{T,S}(\epsilon_F)$, where $\rho_{T,S}(\epsilon_F) = \frac{1}{\pi}\mathrm{Im}G_{T,S}(\epsilon_F)$ denote the LDOS of tip and sample, respectively. (iii) We consider all tunneling channels between the probe particle and individual atoms of the sample as independent. Thus we can write $\Gamma_S = \sum_i \Gamma_i$, where $\Gamma_i = {t_i}^{\dagger}\rho_i(\epsilon_F)t_i$ is the electronic coupling of the ith atom of the sample to the probe particle (see Fig. 1). (iv) We assume that the sample LDOS $\rho_{T,S}(\epsilon)$ is spread homogeneously over all carbon and oxygen atoms of the molecules which make up the sample, i.e., the LDOS $\rho_i(\epsilon_F)$ of all atoms is the same ($\rho_i^{C,O} = \mathrm{const}$). (v) Neither hydrogen atoms of the molecules nor atoms of the metallic substrate are considered. Disregarding the hydrogen atoms is motivated by the fact that the frontier orbitals of large aromatic molecules such as PTCDA are localized mostly on the carbon backbone and on substituents with free electron pairs, while their amplitude on the peripheral hydrogen atoms is negligible (see, e.g., Ref. [30]). (vi) Finally we assume all LDOS $[\rho_P(\epsilon_F),\ \rho_T(\epsilon_F),\ \rho_i(\epsilon_F)]$ to remain constant during the scanning process. Therefore, they are just multiplicative constants which do not affect the tunneling current variation along the tip trajectory. Consequently, the conductance is only a function of the positions of the tip base atom $\vec{r}_T$, surface atoms $\vec{R}_S$ ($\vec{r}_i$ for individual atoms), and the probe particle $\vec{r}_P$:

$$\begin{aligned} dI/dV(\vec{r}_P,\vec{r}_T,\vec{R}_S) &\propto T_T(\vec{r}_P,\vec{r}_T)T_S(\vec{r}_P,\vec{R}_S) \\ &= T_T(\vec{r}_P,\vec{r}_T)\sum_i T_i(\vec{r}_P,\vec{r}_i). \end{aligned} \tag{1}$$

In other words, we can describe the conductance through the probe particle junction via two terms: (a) tunneling from the tip to the probe particle ($T_T \approx {t_T}^{\dagger}t_T$) and (b) subsequent tunneling from the probe particle to the sample ($T_S \approx \sum_i T_i = \sum_i {t_i}^{\dagger}t_i$) (see Fig. 1). The tunneling process T_i between a given sample atom and the probe particle can be expressed as an exponential function $T_i \propto \exp(-\beta_S|\vec{r}_P - \vec{r}_i|)$, where β_S represents the characteristic decay length of the tunneling process between the probe particle and sample atom i. Similarly, we can define $T_T \propto \exp(-\beta_T|\vec{r}_P - \vec{r}_T|)$. An angular momentum dependence of the hopping can also be included (cf. Supplemental Material [25] methods and Fig. 5). Because we are only interested in the variation of the atomic STM contrast due to the probe particle relaxation, we consider for simplicity both characteristic decay lengths β to be independent of the tip-sample distance and equal $\beta_S = \beta_T = 1\,\text{Å}^{-1}$. We can plot maps of the tunneling processes T_S and T_T separately to analyze the effects of tip-probe and sample-probe relaxation qualitatively and irrespective of the sizes of the two β. In reality, β_S and β_T may differ from each other and according to Eq. (1) their relative sizes will influence the relative impact of T_S and T_T on the conductance image.

Clearly, our numerical model omits many processes that happen during tip-sample interaction (e.g., variations of the LDOS or the tunneling barrier, multiple scattering effects, etc. [31]). Moreover, at close tip-sample proximity additional mechanical degrees of freedom of the junction, such as relaxations inside the tip, within the molecular layer and the surface, will eventually become important. Nevertheless, as will be demonstrated here, this simple model accounts for most of the observed contrast features, which proves the crucial importance of probe particle relaxation also for the high-resolution STM contrast.

III. RESULTS AND DISCUSSION

A. High-resolution AFM contrast: Inversion and sharpening

We start the discussion by showing the equilibrium position of the probe particle when a model tip decorated by CO ("CO tip") is scanned over PTCDA molecules in the herringbone monolayer. Figure 2(a) clearly shows that at closer distances the functionalized tip experiences sidewise relaxation. The observed lateral relaxations are induced by the Pauli repulsion that acts at short distances between the probe particle and the atoms of the PTCDA layer: the probe particle tends to relax away from the areas where the Pauli repulsion is strong. According to Fig. 2(a), the Pauli repulsion potential over the PTCDA forms "basins" which become clearly visible as the tip approaches the sample.

Let us now inspect the effect that the tip relaxation has on the frequency shift Δf. The maps of Δf in Fig. 2(b), calculated at the same tip-sample distances as Fig. 2(a), clearly show the *inversion* of the Δf contrast when the tip approaches the sample. Since the observed evolution of the simulated Δf images closely matches the experiment [see Fig. 2(c)], we can identify the mechanism that drives the experimentally observed inversion of the Δf image contrast by analyzing the calculated $F_z(z)$ curves shown in Fig. 2(f).

The two $F_z(z)$ curves calculated for the tip approach over the carbon atom (red) and over the center of the aromatic ring (blue) clearly show that initially the repulsion over the carbon atom increases faster upon tip approach. The situation changes at the distance $z \approx 7.4$Å [Fig. 2(f)] when the probe particle starts to move laterally in order to minimize the effect of the increasing repulsive force. Finally, the repulsion over the ring center becomes stronger, because there the tip is located in the middle of a potential basin that hinders lateral relaxations of the probe particle and thus prevents the relief of the repulsive force.

Comparing the simulated force curves in Fig. 2(f) with corresponding experimental ones reported in Ref. [9], we find that both exhibit a very similar behavior. Small differences between the published experimental $F_z(z)$ curves and the simulated ones shown here can be explained by two facts. First, in our present simulations we do not take into account the attractive interaction between the metal atoms of the tip and the sample. That results in the absence of the attractive force that appears in the experiment after the probe particle has relaxed laterally out of the junction. Secondly, in the simulation we position the tip precisely over the carbon atom and do not take into account the finite amplitude of the qPlus oscillation. This produces a sharp kink in $F_z(z)$ at the moment when the probe particle starts relaxing laterally at the distance $z \approx 7.4$Å [see Fig. 2(f)]. Despite these small and well-understood discrepancies between the experimental and simulated force curves the overall good agreement between both allows us to conclude that the Δf inversion observed both in experiments and simulations occurs due to the decrease of the repulsive force produced by the lateral relaxation of the probe particle in the junction.

Having shown that our model captures the Δf inversion correctly, we note that the inversion effect develops together with a considerable *sharpening* of various features in the Δf images [see the middle and the right panels of Fig. 2(b) and Supplemental Material [25], Video 1]. Hence the evident sharpening of the experimental Δf contrast at closer tip-sample distances can also be attributed to the increasingly pronounced lateral relaxations of the probe particle. More interestingly, sharp lines also become visible in the intermolecular regions, Fig. 2(b), where no covalent bonds exist.

The origin of sharp lines in AFM images between atoms is schematically illustrated in Fig. 3 for the example of the DBTH molecule from Ref. [18], for which such a sharp line is observed between two sulfur atoms which are *not* covalently bonded [see Ref. [18] for the experimental image and Fig. 3(b) (inset) for the simulation]. In Fig. 3(a) the simulated repulsive potential and the attractive basins felt by the probe particle above the DBTH molecule in the vicinity of the two nonbonded sulfur atoms are shown in a three-dimensional plot, together with the trajectories of the probe particle as the tip approaches the sample. One clearly observes a repulsive saddle between the two sulfur-derived hillocks [a cross section through this *smooth* saddle is displayed in the bottom diagram of Fig. 3(b)]. The trajectories in Fig. 3(a) reveal that the probe particle relaxes away from the saddle ridge. This means that, e.g., for the tip position x_{tip} in Fig. 3(b) the probe particle is subject to the repulsive force from the sample at x_{probe}. The mapping of forces at x_{probe} to the macroscopic tip coordinate x_{tip} introduces the sharp ridge in the frequency shift signal Δf that is shown in the upper part of Fig. 3(b), although the surface potential V_{Surf} has a smooth saddle.

The mechanism illustrated in Fig. 3 is operational and leads to sharp lines in the images whenever a repulsive saddle occurs in the potential felt by the probe particle. The origin of this saddle can either be the presence of "real" electron density or the close proximity of atoms. In the case of covalent bonds, the electron density also shows up as a smooth feature in AFM images recorded at large tip distances at which the probe particle does not show appreciable relaxation [first column of Figs. 2(a) and 2(b)]. In the other case, the saddle arises merely from the convolution of the electron densities of the probe particle and the neighboring sample atoms at close tip-sample distances and will disappear for larger distances.

Note that at very close distances the molecular contrast in the experimental images may sometimes become significantly asymmetric; see Fig. 2(c). We attribute this observation to an asymmetry of some of the CO tips. To confirm this hypothesis, we have repeated the simulations using a tilted probe, where the equilibrium position of the probe particle is displaced by 1 Å along y axis away from the lateral position of the tip base. The resulting images show asymmetric contrast on benzene rings and in intermolecular features in good agreement with the experimental findings; see Supplemental Material [25], Fig. 4 and Video 1,2.

B. High-resolution STM contrast on and between molecules

We now analyze the high-resolution STM contrast (i.e., STHM and similar atomic probe contrasts) [6–9]. This contrast has two aspects. On molecules their geometric structure becomes visible, similar to high-resolution AFM [11], while between molecules very pronounced intermolecular features, such as sharp lines between oxygen and hydrogen atoms or sharp-edged trapezoids between the perylene and anhydride sides of two PTCDA molecules, appear [8,9]. The first aspect regularly manifests itself very clearly for H_2-, D_2-, and CO-functionalized tips, whereas the latter is more optimally

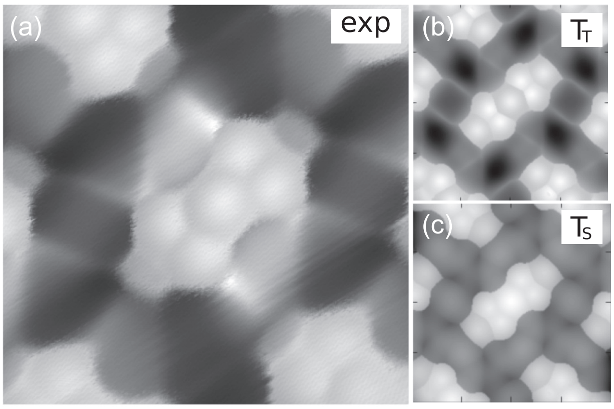

FIG. 4. Intermolecular contrast in high-resolution STM images. (a) Experimental constant height image recorded with a Xe tip over PTCDA/Ag(111). Imaging parameters: area 18 Å × 18 Å; $V = -4$ mV. Prior to the imaging the tip was stabilized at $I = 0.1$ nA and $V = -350$ mV; then the bias was changed to $V = -4$ mV and the tip was moved by 4 Å closer to the surface. (b) Simulated STM image with Xe probe particle (T_T tunneling channel). (c) Simulated STM image with Xe probe particle (T_S tunneling channel). Panels (b) and (c) display approximately the same area as panel (a).

pronounced with H_2, D_2, and Xe tips [9]. As we show now, both aspects of high-resolution STM contrast are closely linked to the same probe particle relaxation that also governs high-resolution AFM images.

First, we focus on the contrast on the molecules, employing exemplary images of PTCDA/Au(111) displayed in Fig. 2(e) that were observed in experiments with a CO-functionalized tip. Using the generic transport model described above, we find that the spatial variation of the tunneling T_S between the probe particle and the sample [Fig. 2(d)] exhibits all essential features of the experimental images in Fig. 2(e). In particular, the overall shape of the molecules and at close distances the appearance of sharp contours between the carbon rings are both reproduced very well. Thus we are led to the conclusion that in this case of a CO tip the experimentally observed high-resolution STM images are mainly determined by the T_S tunneling process.

Turning next to the remarkable STM contrast in the regions between the molecules, we choose the example of a Xe tip (Fig. 4). This time we find excellent agreement between experiment [Fig. 4(a)], carried out on PTCDA/Ag(111), and the simulated image of T_T tunneling [Fig. 4(b)]. Also, the intramolecular contrast (bright aromatic rings with sharp C-C bonds appearing dark) is well reproduced in the T_T channel, although on the molecules the difference between the T_T and T_S images in Fig. 4(b) and Fig. 4(c) is not so large.

Apparently, different experimental situations generate tunneling contrasts of either T_S or T_T type. The obvious questions is why? The variation of the tunneling current in each channel depends exponentially on the distance between the probe particle and the tip base (T_T) or the surface atoms (T_S). In the case of a CO tip, the presence of the stiff covalent bond between CO and the tip base implies only minor changes in the tip-CO distance as the tip is scanned across the sample. Consequently, the T_T channel does not contribute to the STM contrast significantly and the T_S channel prevails.

The situation is different in the case of a Xe tip. The weak interaction (i.e., less stiff bond) between the Xe atom and the tip base leads to more contrast in the T_T channel for Xe than for CO. At the same time, the contrast in the T_S channel will be reduced for Xe relative to CO, for two reasons. First, while CO is electronically more strongly coupled to the tip (i.e., low β) than to the sample, the electronic couplings of the Xe atom to the tip and the sample are expected to be rather comparable; this reduces the relative importance of the coupling to the sample. Secondly and even more importantly, the large atomic radius of Xe smears out the variation of the surface potential, and thus the contrast in T_S, effectively. In conclusion, the mechanically and electronically more weakly coupled part of the junction tends to determine the high-resolution STM image.

C. Can hydrogen bonds be imaged?

The striking AFM/STM contrast between molecules, including the sharp lines observed there, appear suggestive of intermolecular bonds [8,9,16,17,23]. We therefore proceed with addressing in the framework of our mechanical model the imaging of *hydrogen bonds* with AFM that was attributed to the enhanced electron density between oxygen and hydrogen atoms of neighboring molecules [17].

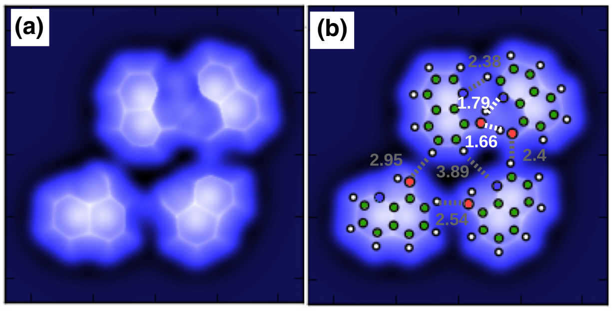

FIG. 5. (Color online) Sharp intermolecular contrast and hydrogen bonds, part I. (a) A simulated AFM image for a 8-hydroxyquinoline tetramer with CO probe particle (tip-sample distance 7.4 Å). The sharp lines in intermolecular regions agree very well with the contrast reported in Fig. 2d of Ref. [17]. (b) Same image as in panel (a), but with a schematic overlay of the molecular structure, with atoms discriminated by colors (white: hydrogen; green: carbon; blue: nitrogen; red: oxygen) and hydrogen bonds (short and strong hydrogen bonds: white; weaker hydrogen bonds: gray). Numbers indicate bond lengths in Å. The image color scale is rescaled by maximum and minimum values of Δf to provide best contrast.

Our previous discussion of the results displayed in Figs. 2, 3, and 4 has shown quite generally that the intermolecular contrast is very closely related to the lateral relaxation of the probe particle. We are therefore led to the suggestion that also the "hydrogen bonds" of Ref. [17] may in fact be due to this effect. To test this conjecture that the observation of *apparent bonds* is in general mainly driven by the relaxation of the probe particle, we have performed AFM simulations for the 8-hydroxyquinoline tetramer (Fig. 5) that was investigated by Zhang *et al.* [17]. The experimental image depicted in Fig. 2B in Ref. [17] should be directly compared to our simulated image at the distance $z = 7.4$ Å [Fig. 5(a)]. Our simulation resolves sharp intermolecular lines connecting typical donors ($-$OH groups) and acceptors (N, O atoms) of hydrogen bonds very well (Fig. 5). According to the mechanism discussed in the context with Fig. 3, these lines are well resolved in our model simply because of the close proximity between donor and acceptor atoms [see white dotted lines in Fig. 5(b) with bond length labels]. Certainly, our purely mechanical model does not have an increased electron density along those lines. On the basis of this finding we suggest that also in the experiments of Zhang *et al.* [17] probe particle relaxation may in fact be the origin of the observed features which the authors identify with hydrogen bonds.

The longer hydrogen bonds between CH groups and O, N atoms [gray dotted lines, Fig. 5(b)], which are less pronounced in Fig. 2B of Ref. [17], become visible in our simulations only at even closer tip-sample proximity (cf. Supplemental Material [25], Fig. 6). This as well as some other minor discrepancies with experimental image (namely the different distortion of aromatic rings) can be explained naturally by two reasons. Firstly, the positions of the atoms in the molecules in our input geometry are probably not exactly the same as in experiment. Secondly, in the experiments, the molecules can move slightly on the surface in both lateral and vertical direction under forces

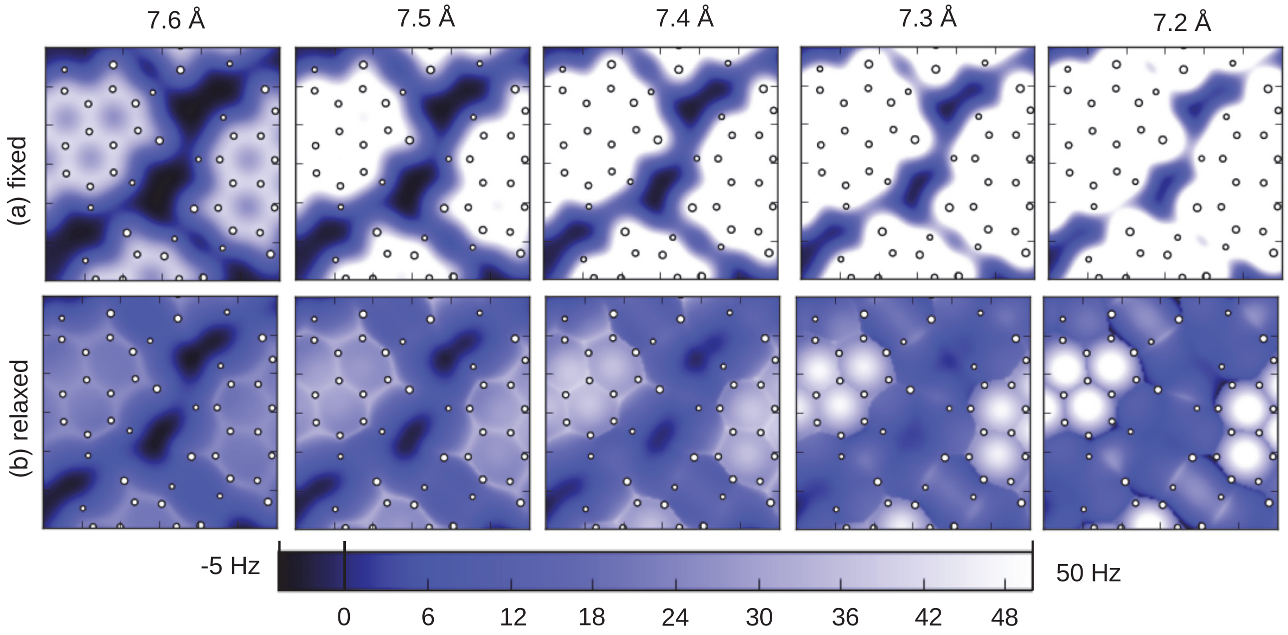

FIG. 6. (Color online) Sharp intermolecular contrast and hydrogen bonds, part II. Simulated AFM images of a monolayer of naphthalene tetracarboxylic diimide (NTCDI) molecules that was studied experimentally by Sweetman *et al.* in Ref. [23]. (a) Without probe particle relaxation; (b) with probe particle relaxation. The images in panel (b) agree very well with experimental AFM images in Figs. 1b and 1c of Ref. [23].

exerted by the tip. These degrees of freedom are not included in our simulation.

Recently an alternative explanation of the origin of the hydrogen bonds was proposed by Sweetman *et al.* [23]. They attribute the imaging mechanism of the hydrogen bonds to a change of the electron density upon tip approach, but without considering image distortions due to tip relaxation. Here we show that although the mechanism discussed in Ref. [23] may be present, it is the probe relaxation which is the driving mechanism that makes the intermolecular bonds visible in the AFM experiment. To do so, we compare experimental AFM images acquired over naphthalene tetracarboxylic diimide (NTCDI) [23] to images that were calculated using our AFM model without [Fig. 6(a)] and with [Fig. 6(b)] probe particle relaxation. Although in both cases we observe an increased repulsion in the region between oxygen and hydrogen atom, only the results obtained with the relaxing probe particle resemble the experimental evidence in Ref. [23]. In simulated images for the fixed probe particle the variation of the repulsion over the bond is very smooth (similar to what is shown in Fig. 4f of Ref. [23]) and the magnitude of the repulsive interaction over hydrogen bonds is much smaller than over the molecule. Only if we take the probe particle relaxation into account are we able to reproduce the sharp contrast visible simultaneously over the molecules and over the intermolecular region in the experiment.

In addition, we note that the observation of an enhanced Pauli repulsion over the area of the hydrogen bond (i.e., between the oxygen and hydrogen atoms of neighboring molecules) in calculations with a rigid probe particle need not be related to an increased electron density in this area. A similar effect is caused by the convolution process due to the finite size of the probe particle, as the following simple consideration shows. For the purpose of the present argument, the Pauli repulsion can be approximated by the overlap of the electron densities of the tip and the sample. Even in the case when there is no electronic density between two atoms on the surface, e.g., the oxygen and hydrogen atoms in a hydrogen bond, a probe particle with a radius that is comparable to the oxygen hydrogen distance will overlap with both surface atoms simultaneously. In AFM imaging, this gives rise to the enhanced repulsion in between the atoms, as a mere consequence of the superposition of the repulsions stemming from both surface atoms. Therefore, it is hard to discriminate the mechanism proposed in Ref. [23] from this straightforward convolution effect that will always be present.

IV. CONCLUSIONS

In conclusion, we have developed a reliable numerical model which despite its simplicity is able to reproduce high-resolution AFM and STM images of molecules, recorded with functionalized tips, very well. The excellent agreement between simulated and experimental images allows us to show that the appearance of sharply resolved structural resolution, observed experimentally both in the AFM and the STM mode, is due to strong lateral relaxations of the probe particle attached to the metallic tip apex. At close tip-sample distances these relaxations follow the potential energy basins produced by the Pauli repulsion. Therefore, sharp features appearing in the images always coincide with the borders of neighboring basins, i.e., the narrow areas where the magnitude and the direction of the lateral relaxation of the probe particle changes strongly upon small variations of the position of the tip relative to the sample. Since the lateral and the vertical relaxations of the probe particle are closely coupled, in the area between the neighboring basins the vertical position of the probe particle also becomes very sensitive to the precise position of the tip, thus producing the sharp image features in the AFM images.

Furthermore, we have also demonstrated that our mechanical model, if combined with a generic model of tunneling through the probe particle junction based on the simplified Landauer formalism, successfully explains the features of high-resolution atomic contrast of STHM. Regarding the STM contrast, we note a few salient points. (1) Any extension of the present tunneling model that includes more realistic charge transport effects will not change its essential feature: namely, that the observed STM contrast is directly related to the relaxation of the probe particle. (2) Our model confirms the concept of the probe particle acting as a combined sensor and transducer [7–9]. This concept relies on the presence of at least one internal degree of freedom in the tunneling junction which can sense a certain physical quantity and transduce this signal into another physical quantity. In the present case, our mechanical model shows how the probe particle senses repulsive forces and by its response to them (mainly lateral relaxation) couples this signal into the tunneling conductance of the junction. (3) The high-resolution AFM and STM imaging mechanism discussed in this paper can be also applied to point contact microscopy [32–34] and contact force microscopy [35,36], as in all the cases sharp features originate from relaxation of the central part of the junction. However, in the present case there is *no hysteresis* in the position of the probe particle as the tip is scanned across the surface. As a consequence, there is also no dependence on scanning direction or speed, and all images can be reconstructed from force vs distance or conductance vs distance curves measured "statically" (as far as the lateral position is concerned) on a grid above the surface.

Finally, we have demonstrated that most sharp image features recorded with functionalized STM/AFM tips, and in particular the resolution obtained in the areas between molecules, do not follow necessarily an increased electron density corresponding to any kind of interatomic or intermolecular bonds, but they trace the sharp boundaries between basins of the short-range repulsive potential produced by atoms that reside close to each other.

ACKNOWLEDGMENTS

P.H. and P.J. acknowledge the support by GAČR, Grant No. 14-16963J, and CAS M100101207. R.T. thanks the Helmholtz Gemeinschaft for financial support in the framework of a Young Investigator Research Group. We thank P. Moriarty (University of Nottingham) and J. Repp (University of Regensburg) for fruitful discussions and valuable comments.

---

[1] G. Binnig, H. Rohrer, C. Gerber, and E. Weibel, Phys. Rev. Lett. **49**, 57 (1982).

[2] G. Binnig, C. F. Quate, and C. Gerber, Phys. Rev. Lett. **56**, 930 (1986).

[3] J. Repp, G. Meyer, S. M. Stojkovic, A. Gourdon, and C. Joachim, Phys. Rev. Lett. **94**, 026803 (2005).

[4] L. Bartels, G. Meyer, K.-H. Rieder, D. Velic, E. Knoesel, A. Hotzel, M. Wolf, and G. Ertl, Phys. Rev. Lett. **80**, 2004 (1998).

[5] L. Gross, N. Moll, F. Mohn, A. Curioni, G. Meyer, F. Hanke, and M. Persson, Phys. Rev. Lett. **107**, 086101 (2011).

[6] R. Temirov, S. Soubatch, O. Neucheva, A. C. Lassise, and F. S. Tautz, New J. Phys. **10**, 053012 (2008).

[7] C. Weiss, C. Wagner, C. Kleimann, M. Rohlfing, F. S. Tautz, and R. Temirov, Phys. Rev. Lett. **105**, 086103 (2010).

[8] G. Kichin, C. Weiss, C. Wagner, F. S. Tautz, and R. Temirov, J. Am. Chem. Soc. **133**, 16847 (2011).

[9] G. Kichin, C. Wagner, F. S. Tautz, and R. Temirov, Phys. Rev. B **87**, 081408 (2013).

[10] F. Giessibl, Rev. Mod. Phys. **75**, 949 (2003).

[11] L. Gross, F. Mohn, N. Moll, P. Liljeroth, and G. Meyer, Science **325**, 1110 (2009).

[12] L. Gross, F. Mohn, N. Moll, B. Schuler, A. Criado, E. Guitián, D. Peña, A. Gourdon, and G. Meyer, Science **337**, 1326 (2012).

[13] N. Moll, L. Gross, F. Mohn, A. Curioni, and G. Meyer, New J. Phys. **12**, 125020 (2010).

[14] M. P. Boneschanscher, S. K. Hämäläinen, P. Liljeroth, and I. Swart, ACS Nano **8**, 3006 (2010).

[15] M. Neu, N. Moll, L. Gross, G. Meyer, F. J. Giessibl, and J. Repp, Phys. Rev. B **89**, 205407 (2014).

[16] C. Weiss, C. Wagner, R. Temirov, and F. S. Tautz, J. Am. Chem. Soc. **132**, 11864 (2010).

[17] J. Zhang, P. Chen, B. Yuan, W. Ji, Z. Cheng, and X. Qiu, Science **342**, 611 (2013).

[18] N. Pavliček, C. Herranz-Lancho, B. Fleury, M. Neu, J. Niedenführ, M. Ruben, and J. Repp, Phys. Status Solidi B **250**, 2424 (2013).

[19] L. Kilian, E. Umbach, and M. Sokolowski, Surf. Sci. **600**, 2633 (2006).

[20] G. Mercurio, O. Bauer, M. Willenbockel, N. Fairley, W. Reckien, C. H. Schmitz, B. Fiedler, S. Soubatch, T. Bredow, M. Sokolowski, and F. S. Tautz, Phys. Rev. B **87**, 045421 (2013).

[21] P. Jelínek, H. Wang, J. P. Lewis, O. F. Sankey, and J. Ortega, Phys. Rev. B **71**, 235101 (2005).

[22] J. P. Lewis, P. Jelínek, J. Ortega, A. A. Demkov, D. G. Trabada, B. Haycock, H. Wang, G. Adams, J. K. Tomfohr, E. Abad, H. Wang, and D. A. Drabold, Phys. Status Solidi B **248**, 1989 (2011).

[23] A. M. Sweetman, S. P. Jarvis, H. Sang, I. Lekkas, P. Rahe, Y. Wang, J. Wang, N. R. Champness, L. Kantorovich, and P. Moriarty, Nat. Commun. **5**, 3931 (2014).

[24] W. L. Jorgensen and J. Tirado-Rives, J. Am. Chem. Soc. **110**, 1657 (1988).

[25] See Supplemental Material at http://link.aps.org/supplemental/10.1103/PhysRevB.90.085421 for (i) additional figures regarding the robustness of the model, the influence of tip asymmetry and orbital symmetries on the simulated images, and the imaging of hydrogen bonds, (ii) for more details on the simulation method, and (iii) for two videos showing the evolution of simulated AFM images as the tip approaches the surface.

[26] F. Mohn, B. Schuler, L. Gross, and G. Meyer, Appl. Phys. Lett. **102**, 073109 (2013).
[27] F. Mohn, J. Repp, L. Gross, G. Meyer, M. S. Dyer, and M. Persson, Phys. Rev. Lett. **105**, 266102 (2010).
[28] J. E. Sader and S. P. Jarvis, Appl. Phys. Lett. **84**, 1801 (2004).
[29] R. Landauer, IBM J. Res. Dev. **1**, 223 (1957).
[30] M. Rohlfing, R. Temirov, and F. S. Tautz, Phys. Rev. B **76**, 115421 (2007).
[31] P. Jelínek, M. Ondráček, and F. Flores, J. Phys.: Condens. Matter **24**, 084001 (2012).
[32] J. A. Stroscio and R. J. Celotta, Science **306**, 242 (2004).
[33] Y.-H. Zhang, P. Wahl, and K. Kern, Nano Lett. **11**, 3838 (2011).
[34] G. Schull, Y. J. Dappe, C. González, H. Bulou, and R. Berndt, Nano Lett. **11**, 3142 (2011).
[35] H. Hölscher, U. D. Schwarz, O. Zwörner, and R. Wiesendanger, Phys. Rev. B **57**, 2477 (1998).
[36] H. Hölscher, U. Schwarz, and R. Wiesendanger, Europhys. Lett. **36**, 19 (1996).

Origin of High-Resolution IETS-STM Images of Organic Molecules with Functionalized Tips

Prokop Hapala,[1,*] Ruslan Temirov,[2,3] F. Stefan Tautz,[2,3] and Pavel Jelínek[1,4,†]
[1]*Institute of Physics, Academy of Sciences of the Czech Republic, v.v.i., Cukrovarnická 10, 162 00 Prague, Czech Republic*
[2]*Peter Grünberg Institut (PGI-3), Forschungszentrum Jülich, 52425 Jülich, Germany*
[3]*Jülich Aachen Research Alliance (JARA)–Fundamentals of Future Information Technology, 52425 Jülich, Germany*
[4]*Graduate School of Engineering, Osaka University 2-1, Yamada-Oka, Suita, Osaka 565-0871, Japan*

(Received 12 September 2014; revised manuscript received 17 October 2014; published 25 November 2014)

Recently, the family of high-resolution scanning probe imaging techniques using decorated tips has been complemented by a method based on inelastic electron tunneling spectroscopy (IETS). The new technique resolves the inner structure of organic molecules by mapping the vibrational energy of a single carbon monoxide (CO) molecule positioned at the apex of a scanning tunneling microscope (STM) tip. Here, we explain high-resolution IETS imaging by extending a model developed earlier for STM and atomic force microscopy (AFM) imaging with decorated tips. In particular, we show that the tip decorated with CO acts as a nanoscale sensor that changes the energy of its frustrated translation mode in response to changes of the local curvature of the surface potential. In addition, we show that high resolution AFM, STM, and IETS-STM images can deliver information about the charge distribution within molecules deposited on a surface. To demonstrate this, we extend our mechanical model by taking into account electrostatic forces acting on the decorated tip in the surface Hartree potential.

DOI: 10.1103/PhysRevLett.113.226101 PACS numbers: 68.37.Ef, 68.37.Ps, 68.43.Fg

One of the most exciting and significant breakthroughs in the field of scanning probe microscopy in the last years is undoubtedly the achievement of high-resolution STM [1] and AFM [2] images of molecular structures with functionalized tips [3–5]. In general, the high-resolution images, being typically acquired in the regime where the tip-surface interaction becomes repulsive, are characterized by the presence of sharp features in both intra- and intermolecular regions. The sharp ridges observed in the intramolecular region often mimic the internal molecular structure [4,6], with only a few exceptions [7,8]. The capability of AFM/STM to resolve internal atomic and chemical structures in real space opened new horizons for the characterization of molecules and surfaces at the atomic scale [6,9–17].

The origin of the high resolution of molecular structures in AFM and STM images has been attributed to Pauli repulsion [2,4,18] and the bending of the functionalized tip apex [6]. Recently, we introduced a simulation model which provides a unified insight into the detailed mechanism of the high-resolution imaging with decorated tips in both AFM and STM [8]. According to the model, the decorated tip apex acts as a nanoscale force sensor that responds with significant relaxations of the decorating particle (probe particle) towards local minima of the tip-sample interaction potential at close distances. These relaxations cause kinks in both the frequency shift and the tunneling current signals and thus become observable in AFM and STM images as sharp contrast features [8]. Although the model of Ref. [8] was originally used to confirm the decisive role of Pauli repulsion in high-resolution STM and AFM imaging of molecular structures with functionalized tips, it must be noted that imaging of other types of interactions (e.g., electrostatic) should also be possible. Namely, the influence of the intramolecular charge distribution [19] on the molecular contrast has not been analyzed in detail yet.

Inelastic electron tunneling spectroscopy (IETS) [20] is a well-established technique, which has been used to perform, e.g., chemical identification [21] or reaction [22–24] and molecular manipulation [25]. Very recently, Chiang *et al.* [26] introduced a novel approach of high-resolution molecular imaging by means of IETS. They obtained high-resolution images of a cobalt-phthalocyanine (CoPc) molecule deposited on the Ag(110) surface by mapping the IETS feature corresponding to the frustrated translation vibrational mode of a CO molecule attached to the STM tip. The IETS-STM maps of Chiang *et al.* show the sharply resolved structure of the molecular skeleton (i.e., the positions of atoms and bonds), very similar to the high-resolution AFM/STM images with functionalized tips [1,2]. Also the constant-height STM image recorded during IETS mapping (see Fig. S4 in Ref. [26]) shows characteristic sharp contrast features similar to those observed in earlier STM experiments [1,4,27]. Further proliferation of the IETS-STM imaging method, as well as the precise interpretation of the experimental results, strongly depends on a detailed understanding of the imaging mechanism. However, the underlying mechanism of the high-resolution IETS-STM images has not been addressed yet.

In this Letter, we provide an explanation of the origin of the high-resolution IETS-STM images of Ref. [26]. We show how the frequency of the frustrated translation mode of the probe particle terminating the tip is influenced by changes of the surface potential. The IETS-STM imaging can thus be seen as another utilization of the nanoscale sensor functionality of the decorated tip [4], mapping the interactions between the tip and the surface and transducing it—in this case—into the characteristic IETS signal. We also extend our AFM/STM simulation model [8] by including the electrostatic force acting on the functionalized probe in the surface Hartree potential. This allows us to analyze in detail the influence of electrostatic forces on high-resolution images. By applying the extended model to the analysis of the IETS-STM images of CoPc/Ag(110) reported by Chiang *et al.* [26], we demonstrate that the decorated tip is also sensitive to the electrostatic interaction between a charge localized on the tip apex and an electrostatic polarization generated by the inhomogeneous charge distribution inside the CoPc molecule.

We start by briefly summarizing the basic ingredients of our mechanical model; for details, see Ref. [8]. A single atom or a small molecule decorating the apex of a metal tip is modeled by a single point particle interacting via van der Waals attraction and Pauli repulsion with the atoms of the surface and the metallic tip apex atom. These interactions are described by empirical pairwise Lennard-Jones (LJ) potentials. The repulsive branch of the LJ potential describes the Pauli repulsion that plays the key role in the high-resolution imaging. Additionally, in order to simulate the cylindrical confinement potential of the tip, the movement of the probe particle is constrained by a lateral harmonic potential below the metallic tip apex. The harmonic potential determines the lateral "bending" stiffness k of the functionalized tip.

On top of the mechanical model we simulate the STM images by computing the tunneling current through the junction at each lateral position of the tip as a two-step tunneling process between the tip and the probe particle and further between the probe particle and the sample. As it has been shown previously [8], our model reproduces all essential features of experimental high-resolution AFM/STM images very well. More details about the model and its comparison with experimental evidence can be found in Ref. [8].

To address the IETS-STM experiments of Ref. [26], we have extended our model to include a calculation of the vibrational energy levels ϵ of the probe particle. In addition, we have included the previously neglected electrostatic force which stems from the Coulombic interaction between the internal charge distribution on a surface or in a molecule and a charge cloud localized on the probe particle. For the detailed description of the new model see the Supplemental Material [28].

For didactic purposes, we first illustrate on a simplified model how the interaction with a surface atom influences vibration modes of the probe particle. In this model the probe particle can move just in one dimension (x_{PROBE}) while it is fixed at a particular distance (z_{PROBE}) from the single atom on the surface. The overall potential felt by the probe particle is given by two contributions: (i) the harmonic potential, which simulates bending stiffness of the probe particle [see V_{SPRING} in Fig. 1(a)] and (ii) the van der Waals and Pauli potentials acting between the probe particle and the surface atom modeled by the LJ potential

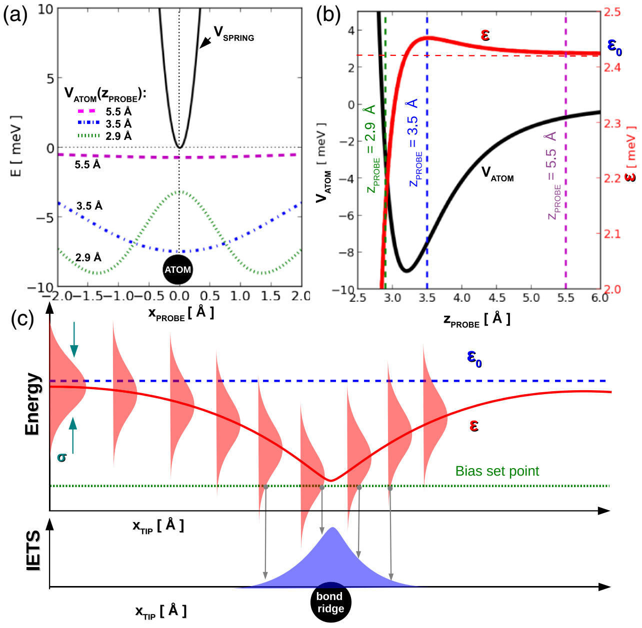

FIG. 1 (color online). 1D IETS-STM model. (a) Individual contributions to the potential energy of the probe particle, plotted as a function of its lateral position x_{PROBE}: The full line shows the harmonic potential of the tip (V_{SPRING}) responsible for the lateral confinement of the probe particle beneath the apex. The dashed lines show the L-J potential of the interaction of the probe particle with the surface atom (V_{ATOM}) or three different distances between probe particle and surface z_{PROBE}= 5.5 Å (pink dashed line), 3.5 Å (blue dash-dot line) and 2.9 Å (green dotted line). (b) Corresponding evolution of the vibration energy eigenvalue ϵ of the probe particle (red line) and probe particle potential energy V_{ATOM} (black line) as a function of z_{PROBE}. Relaxations of the probe particle are not taken into the account in the model. (c) Schematic explanation how the variation of the vibration energy eigenvalue ϵ (red line) affects the intensity of the IETS-STM signal (blue peak) when the tip scans over a surface protrusion (e.g. a bond ridge or an atom). At close tip-surface distances (repulsive regime), the proximity of the surface atom/bond ridge produces a softening of the vibration energy ϵ with respect to the unperturbed vibration energy ϵ_0 (dashed blue line). Thus the characteristic IETS peak [21] (represented by the red gaussian) centered at the vibration energy ϵ crosses the bias set point (green line) at a certain x_{TIP} accordingly changing the IETS-STM signal (blue peak). We used L-J parameters of oxygen atom for both probe particle and surface atom (see [28]) for (a),(b).

[V_{ATOM} in Figs. 1(a) and 1(b)]. For simplicity, the LJ potential between the probe particle and the tip apex atom is neglected in the didactic one-dimensional model; instead, the probe particle is constrained to a fixed z_{PROBE}. Note, however, that in our full 3D simulations this potential is included.

The red line in Fig. 1(b) shows the variation of the vibrational energy ε with the distance z_{PROBE}. In the far distance regime, e.g., at $z_{\mathrm{PROBE}} = 5.5$ Å, the interaction with the substrate is negligible. Therefore, the potential affecting the motion of the probe particle is entirely determined by the lateral harmonic potential of the tip. In our simulations we set the stiffness of this potential to $k = 1.44$ N/m. This provides a vibrational energy of the frustrated translation mode of 2.4 meV, which is in good agreement with the experimental observation [26]. The chosen k corresponds well to the upper range predicted for CO-terminated tips (see the supplementary section of Ref. [6]).

At intermediate distances, e.g., $z_{\mathrm{PROBE}} = 3.5$ Å, the presence of the attractive surface potential with convex curvature increases slightly the vibration energy ε (by < 0.1 meV). On the other hand, at close distances, e.g., $z_{\mathrm{PROBE}} = 2.9$ Å, the surface potential becomes repulsive with a distinct concave curvature near the maximum at the position of the surface atom [see the dashed green line in Fig. 1(a)]. This leads to a considerable softening (by ≈ 0.3 meV) of the vibration energy ε.

If we approach even closer towards the surface atom, the curvature of the total potential would become negative, leading to an unphysical imaginary vibration frequency. At these distances, it is thus necessary to consider the relaxation of the probe particle into a new local minimum to obtain physically meaningful results.

Let us generalize this observation to a 2D situation, where the tip scans in a lateral direction over a molecule at a close distance. In this case, the repulsion and, hence, the concave curvature of the surface potential is highest in areas directly above the molecular skeleton (i.e., local maxima and saddles). Figure 1(c) displays schematically the variation of the frustrated translation vibrational energy ε when the tip moves laterally across a bond or atom of the molecule. We see that ε and, consequently, the position of the IETS peak [29] decrease as the probe particle approaches the bond or atom, with a sharp minimum just above them. Therefore, the lateral mapping of the IETS peak intensity, recorded at a properly selected bias voltage [indicated by the dashed green line in Fig. 1(c)], gives rise to an image contrast that exhibits significant variations over bonds and atoms. This explains why in the experiment bond ridges appear bright in the IETS signal [26]. However, we should stress that in the above analysis we have not yet taken into account the probe particle relaxation. As we will demonstrate later, the probe particle relaxation leads to a considerable sharpening of the IETS-STM contrast, as in the case of high-resolution AFM and STM imaging [6,8] (see also the Supplemental Material [28]).

Now we benchmark our model against experimental results of a CoPc molecule deposited on a Ag(110) surface [26]. First, we carry out total energy DFT calculations with the VASP code in order to obtain an optimized structure of the adsorbed molecule. A detailed description of the DFT calculations can be found in the Supplemental Material [28]. According to the DFT calculations, the molecule is located ≈ 3 Å above the surface and the Co and N atoms bend slightly downward, establishing a chemical bond with Ag atoms underneath. On the other hand, the outer benzene rings move slightly upward so that the molecular buckling is ≈ 0.6 Å.

More importantly, the DFT simulation indicates a substantial charge redistribution within the CoPc molecule. The Hartree potential shown in Fig. 2 reveals a positive potential over the pentagonal pyrrole ring and a negative potential over the imine nitrogens. In order to account for the possible effects caused by the charge redistribution inside CoPc, we extend the original model [8] by including the electrostatic interactions between the probe particle and the surface. The electrostatic force is evaluated from the Hartree surface potential obtained from DFT calculations and a preselected charge density on the probe particle (for details see the Supplemental Material [28]). As will be shown below, the inclusion of electrostatic interactions between the tip and the surface is vital for understanding the experimental IETS-STM contrast.

A detailed analysis of the experimental IETS-STM images of the CoPc molecule reveals an enlargement of the pyrrole rings together with a contraction of the area corresponding to the imine nitrogens in the central part of

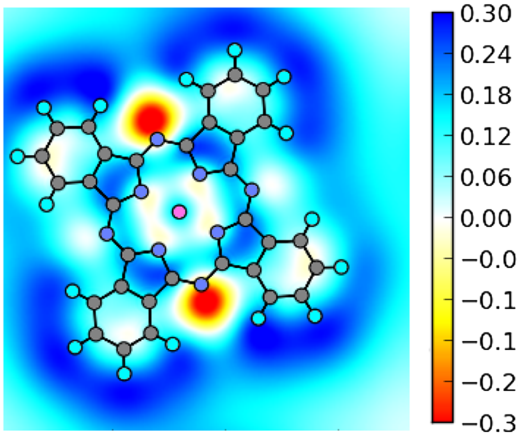

FIG. 2 (color online). Hartree potential of a CoPc molecule adsorbed on Ag(110), obtained from DFT calculations in the xy plane 2.00 Å above the Co atom of the molecule. The Hartree potential reveals substantial partial charging between the pyrrole rings and imine nitrogens. Color scale bar in eV. The following color code for atoms is used: N: blue, C: gray, H: turquoise, Co: pink.

the molecule (see Fig. 3 in Ref. [26]). This is the area where the Hartree potential rapidly changes its sign (see Fig. 2). Figure 3 shows our simulated constant-height IETS-STM images obtained with the extended simulation model, including the electrostatic interactions for different values of charge located on the probe particle. We see that the inclusion of the electrostatic interaction distorts the molecular contrast in the central part of the molecule (the red line in Fig. 3 depicts the molecular skeleton of the relaxed molecule). The calculated IETS-STM image [Fig. 3(a)] obtained with the negatively charged probe particle $Q = -0.4e$ matches very well the experimental evidence (compare to Fig. 3A in Ref. [26]). Alternatively, the presence of the positive charge $Q = +0.4e$ on the probe particle leads to an opposite effect as visible in Fig. 3.

We note that our simulated constant-height IETS-STM images display a more pronounced contrast on the outer benzene rings compared to the experiment [26]. This discrepancy can be explained by the large flexibility of the outer benzene rings. According to our DFT simulations, the benzene rings are only weakly coupled to the silver surface. Thus, when the tip operates in the repulsive regime, one can expect the flexible benzene rings of CoPc to bend down under the force exerted by the tip. We assume this bending to be responsible for the reduced resolution over the benzene rings in the experiment. In the IETS-STM simulation, in contrast, the atomic structure of the molecule on the surface is fixed rigidly; this gives rise to the enhanced atomic contrast over the benzene rings in comparison with experiment.

Finally we compare the different channels (AFM, STM, and IETS) calculated with our simulation model, including the electrostatic distortion correction considering the probe particle with a negative charge of $-0.4e$. Figure 4(a) illustrates the relaxation of the probe particle due to the interaction with the surface, which is responsible for the distortion and sharpening of AFM/STM images as discussed in Refs. [6,8]. In the far distance regime, where the probe particle does not relax, the molecular contrast is blurred in all channels. The situation changes when the probe particle starts to move towards the local minima of the surface potential, producing the sharpening of both the STM and AFM contrasts, followed by the characteristic AFM signal inversion between the atoms or bonds and the rings [8]. Simultaneously with the sharpening of the STM and AFM contrasts and the inversion of the AFM contrast we observe a considerable sharpening of the contrast in the IETS-STM channel, which unambiguously proves the importance of the probe particle relaxation also for the increased resolution observed in the experimental IETS-STM images.

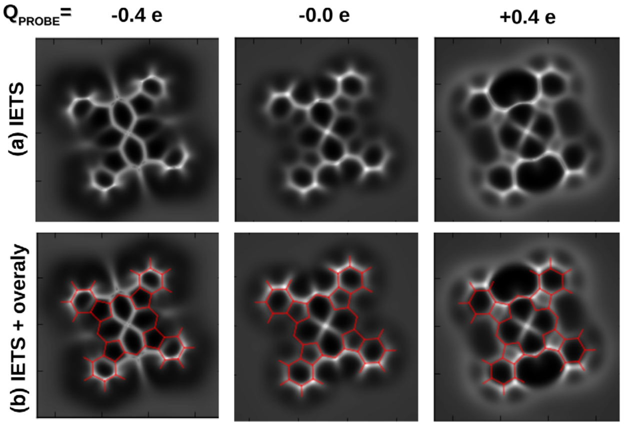

FIG. 3 (color online). Simulated constant-height IETS-STM images calculated at tip-sample distance $z = 7.3$ Å at $V = 1.5$ mV for different point charge values on the probe particle, $Q = -0.4e$, 0, and $+0.4e$. (a) IETS-STM images. (b) The same images as in panel (a), overlaid with the molecular skeleton (red line) of the relaxed CoPc molecule on Ag(110) obtained by the DFT calculations. Bright color indicates a large intensity of the IETS signal; see [29].

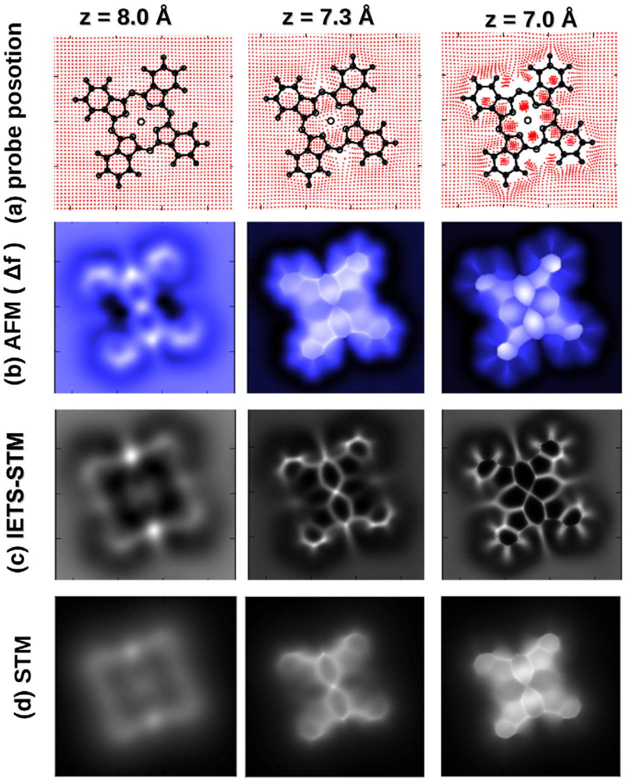

FIG. 4 (color online). Simulated constant-height AFM, STM, and IETS-STM images obtained with the extended simulation model assuming probe particle charge of $-0.4e$. (a) Red dots indicate the relaxed xy position of the probe particle; AFM (b), IETS-STM (c), and STM (d) channels for different tip-sample distances $z = 8.0$, 7.3, and 7.0 Å are shown. Color scales in all images except (a) are renormalized to obtain the best molecular contrast.

We stress that the pattern of the calculated constant-height IETS-STM image at the far tip-sample distance $z = 8$ Å shown in Fig. 4(c) coincides very well with the

Hartree potential projected in the same z plane (see Fig. 3). This means that for these distances the shape of the tip-sample potential energy is determined mostly by the electrostatic interaction. Consequently, IETS-STM images acquired at far distances map directly the variation of the surface electrostatic potential at the given z.

To summarize, we have shown that the frustrated translation of the CO molecule at the tip apex reacts sensitively to the changes of local curvature of the surface potential. Namely, the attractive (convex) and repulsive (concave) character of the surface potential induces vibration mode hardening and softening, respectively. Detection of the resultant variations of the vibrational energy by the standard technique of IETS-STM allows one to map laterally the curvature of the surface potential. Since the curvature of the surface potential changes strongly in the vicinity of the atoms and interatomic bonds, the obtained maps are expected to be closely related to the underlying structure of the scanned surface. Furthermore, we have shown that the structural resolution obtained by lateral mapping of the IETS-STM signal is further sharpened by the lateral relaxations of the particle decorating the tip that occurs under the influence of the repulsive forces acting on it from the surface. This mechanism puts AFM, STM, and IETS-STM imaging with modified tips on a common ground. Finally, we have demonstrated that decorated tips can also be used to image local distributions of electrostatic charge. Eventually, this observation may be useful for the development and understanding of imaging techniques yielding better spacial resolution than the traditional AFM-based Kelvin probe force microscopy [19]. We believe that a detailed understanding of the IETS imaging mechanism and the influence of the internal charge distribution on the high-resolution images will contribute to further proliferate scanning probe microscopy techniques.

P. H. and P. J. acknowledge the support by GAČR, Grant No. 14-16963J and EMRP SIB611 CRYSTAL.

---

[*]Corresponding author.
hapala@fzu.cz
[†]jelinkep@fzu.cz

[1] R. Temirov, S. Soubatch, O. Neucheva, a. C. Lassise, and F. S. Tautz, New J. Phys. **10**, 053012 (2008).

[2] L. Gross, F. Mohn, N. Moll, P. Liljeroth, and G. Meyer, Science **325**, 1110 (2009).

[3] L. Bartels, G. Meyer, K.-H. Rieder, D. Velic, E. Knoesel, A. Hotzel, M. Wolf, and G. Ertl, Phys. Rev. Lett. **80**, 2004 (1998).

[4] C. Weiss, C. Wagner, C. Kleimann, M. Rohlfing, F. S. Tautz, and R. Temirov, Phys. Rev. Lett. **105**, 086103 (2010).

[5] G. Kichin, C. Weiss, C. Wagner, F. S. Tautz, and R. Temirov, J. Am. Chem. Soc. **133**, 16 847 (2011).

[6] L. Gross, F. Mohn, N. Moll, B. Schuler, A. Criado, E. Guitián, D. Peña, A. Gourdon, and G. Meyer, Science **337**, 1326 (2012).

[7] N. Pavliček, C. Herranz-Lancho, B. Fleury, M. Neu, J. Niedenführ, M. Ruben, and J. Repp, Phys. Status Solidi B **250**, 2424 (2013).

[8] P. Hapala, G. Kichin, C. Wagner, F. S. Tautz, R. Temirov, and P. Jelínek, Phys. Rev. B **90**, 085421 (2014).

[9] S. Kawai, A. Sadeghi, X. Feng, P. Lifen, R. Pawlak, T. Glatzel, A. Willand, A. Orita, J. Otera, S. Goedecker, and E. Meyer, ACS Nano **7**, 9098 (2013).

[10] M. Neu, N. Moll, L. Gross, G. Meyer, F. J. Giessibl, and J. Repp, Phys. Rev. B **89**, 205407 (2014).

[11] J. Welker and F. J. Giessibl, Science **336**, 444 (2012).

[12] Z. Sun, M. P. Boneschanscher, I. Swart, D. Vanmaekelbergh, and P. Liljeroth, Phys. Rev. Lett. **106**, 046104 (2011).

[13] I. Swart, L. Gross, and P. Liljeroth, Chem. Commun. (Cambridge) **47**, 9011 (2011).

[14] L. Gross, N. Moll, G. Meyer, R. Ebel, W. M. Abdel-Mageed, and M. Jaspars, Nat. Chem. **2**, 821 (2010).

[15] A. Riss, S. Wickenburg, P. Gorman, L. Z. Tan, H.-Z. Tsai, D. G. de Oteyza, Y.-C. Chen, A. J. Bradley, M. M. Ugeda, G. Etkin, S. G. Louie, F. R. Fischer, and M. F. Crommie, Nano Lett. **14**, 2251 (2014).

[16] M. P. Boneschanscher, S. K. Hämäläinen, P. Liljeroth, and I. Swart, ACS Nano **8**, 3006 (2014).

[17] C. Weiss, C. Wagner, R. Temirov, and F. S. Tautz, J. Am. Chem. Soc. **132**, 11 864 (2010).

[18] N. Moll, L. Gross, F. Mohn, A. Curioni, and G. Meyer, New J. Phys. **12**, 125020 (2010).

[19] F. Mohn, L. Gross, N. Moll, and G. Meyer, Nat. Nanotechnol. **7**, 227 (2012).

[20] R. C. Jaklevic and J. Lambe, Phys. Rev. Lett. **17**, 1139 (1966).

[21] B. C. Stipe, M. A. Rezaei, and W. Ho, Science **280**, 1732 (1998).

[22] J. I. Pascual, N. Lorente, Z. Song, H. Conrad, and H. P. Rust, Nature (London) **423**, 525 (2003).

[23] B. C. Stipe, M. A. Rezaei, W. Ho, S. Gao, M. Persson, and B. I. Lundqvist, Phys. Rev. Lett. **78**, 4410 (1997).

[24] S. Katano, Y. Kim, M. Hori, M. Trenary, and M. Kawai, Science **316**, 1883 (2007).

[25] B. C. Stipe, Science **279**, 1907 (1998).

[26] C. l. Chiang, C. Xu, Z. Han, and W. Ho, Science **344**, 885 (2014).

[27] G. Kichin, C. Wagner, F. S. Tautz, and R. Temirov, Phys. Rev. B **87**, 081408 (2013).

[28] See Supplemental Material at http://link.aps.org/supplemental/10.1103/PhysRevLett.113.226101 for more details, which includes Refs. [30–34].

[29] For simplicity we simulate the IETS signal as a gaussian peak in d^2I/dV^2 centered around the vibration energy ε with a fixed width $\sigma = 0.7$ meV, which fits well the experimental evidence.

[30] G. Kresse and J. Furthmüller, Phys. Rev. B **54**, 11 169 (1996).

[31] J. P. Perdew, J. A. Chevary, S. H. Vosko, K. A. Jackson, M. R. Pederson, D. J. Singh, and C. Fiolhais, Phys. Rev. B **46**, 6671 (1992).

[32] D. Vanderbilt, Phys. Rev. B **41**, 7892 (1990).

[33] S. Grimme, J. Comput. Chem. **27**, 1787 (2006).

[34] S. S. Batsanov, J. Mol. Struct. **990**, 63 (2011).

Probing Charges on the Atomic Scale by Means of Atomic Force Microscopy

F. Albrecht and J. Repp[*]
Institute of Experimental and Applied Physics, University of Regensburg, 93053 Regensburg, Germany

M. Fleischmann and M. Scheer
Institute of Inorganic Chemistry, University of Regensburg, 93053 Regensburg, Germany

M. Ondráček and P. Jelínek
Institute of Physics of the Academy of Sciences of the Czech Republic, 16253 Prague, Czech Republic

(Received 27 February 2015; revised manuscript received 1 July 2015; published 13 August 2015)

Kelvin probe force spectroscopy was used to characterize the charge distribution of individual molecules with polar bonds. Whereas this technique represents the charge distribution with moderate resolution for large tip-molecule separations, it fails for short distances. Here, we introduce a novel local force spectroscopy technique which allows one to better disentangle electrostatic from other contributions in the force signal. It enables one to obtain charge-related maps at even closer tip-sample distances, where the lateral resolution is further enhanced. This enhanced resolution allows one to resolve contrast variations along individual polar bonds.

DOI: 10.1103/PhysRevLett.115.076101 PACS numbers: 68.37.-d, 68.43.-h

The use of a well-defined functionalization of a scanning probe tip with one CO molecule has enabled submolecular resolution in frequency-modulated atomic force microscopy (FM-AFM) resolving the chemical structure of individual molecules [1]. Since then, this technique has been widely applied [2–10]. AFM-based Kelvin probe force spectroscopy (KPFS) [11] provides the local contact potential difference (LCPD) between tip and sample [12–14]. As surface charges and dipoles affect the local work function, LCPD is intimately linked to the charge distribution at surfaces [15,16] such that KPFS can be used to determine the charge state of individual atoms [17] and molecules [18], for example. Hence, the use of tip functionalization in KPFS promises the mapping of charge distributions at ultimate resolution and inside molecules, which is key to the understanding of basic processes in many fields, e.g., organic photovoltaics. Mapping of the quadrupole moment in a molecular switch [4] and of the dipole moment in donor-acceptor molecules [10] has been achieved with CO-terminated AFM tips recently. However, in order to attain charge resolution at the level of individual bonds, the probe has to be brought so close to the sample that other force contributions also become important. In this regime, KPFS maps have shown a contrast inversion [10] which hints that they may not reflect the charge distribution anymore [10].

Here we study trimeric perfluoro-ortho-phenylene mercury ($F_{12}C_{18}Hg_3$) and its hydrogen-terminated counterpart $H_{12}C_{18}Hg_3$, exhibiting bonds of different polarities and intramolecular charge distributions. By analyzing distance-dependent KPFS maps of these along with the residuals from fits, we show that KPFS fails to reproduce LCPD in the very-close-distance regime. We identify one physical reason for this limitation of KPFS, which lies in the bias dependence of nonelectrostatic short-range force contributions. To overcome this constraint, we propose a novel FM-AFM-based technique to detect the charge distribution on atomic scales. It exploits the dependence of the electric field on tip-sample distance to map out the charge distribution at highest resolution. At intermediate distances, at which KPFS works reliably, it was tested for several different molecules in comparison to KPFS maps. The novel technique allows one to extend the mapping to even closer distances, where KPFS fails. In this regime, we investigate the charge distribution in $F_{12}C_{18}Hg_3$ and $H_{12}C_{18}Hg_3$, for which contrast changes along individual polar bonds could be resolved.

Experiments were performed using a homebuilt qPlus-based [19] FM-AFM [20] in ultrahigh vacuum ($p \approx 5 \times 10^{-11}$ mbar) at low temperatures of $\simeq 5$ K including scanning-tunneling functionality. All investigations of $F_{12}C_{18}Hg_3$, $H_{12}C_{18}Hg_3$, and perylene-3,4,9,10-tetracarboxylic dianhydride (PTCDA) were performed with the molecules directly adsorbed on Cu(111), whereas 10-chloro-anthracene-9-carbonitrile (ClAnCN) was studied on a double layer of NaCl on Cu(111). The tip was functionalized with a CO molecule, and bias voltages refer to the sample with respect to the tip. All AFM data were obtained at 0.5 Å oscillation amplitude, and all images and KPFS maps were acquired in constant-height mode. Calculations of $F_{12}C_{18}Hg_3$ and $H_{12}C_{18}Hg_3$ on Cu(111) are based on total-energy density-functional theory (DFT) [21] (for details, see Ref. [22]).

To unambiguously relate the experimental data to the polar nature of bonds, we compared $F_{12}C_{18}Hg_3$ and $H_{12}C_{18}Hg_3$ molecules adsorbed next to each other in the same data set, acquired with the very same tip apex.

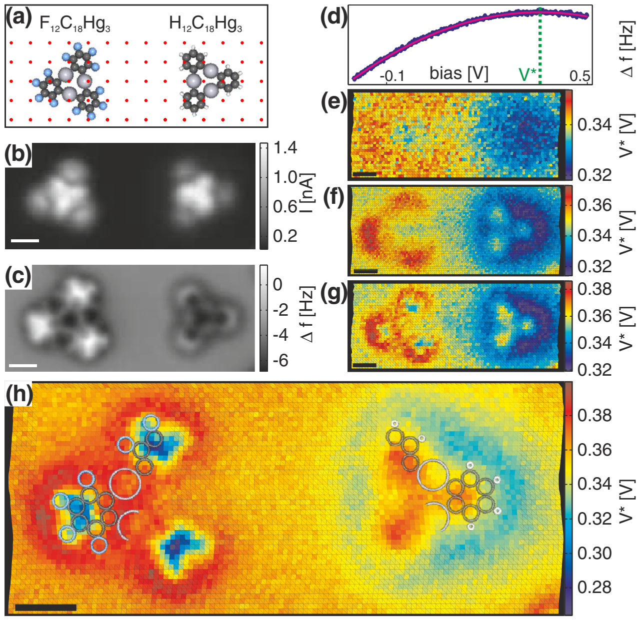

FIG. 1 (color online). KPFS on grids on individual $F_{12}C_{18}Hg_3$ and $H_{12}C_{18}Hg_3$ molecules. (a) Ball models of $F_{12}C_{18}Hg_3$ (left-hand side) and $H_{12}C_{18}Hg_3$ (right-hand side) shown in the same orientation as the molecules under investigation. Carbon, mercury, hydrogen, and fluorine atoms are represented in black, gray, white, and blue, respectively. At each point of a dense grid over the molecules (schematically indicated by red dots), individual spectra are acquired. (b) Current image of the two molecules ($z = 9.6$ Å [22], $V = 0.2$ V). (c) Δf image ($z = 9.0$ Å). (d) Exemplary KPFS spectrum (blue) of one grid point with parabolic fit (pink) from which $V^\star$ is extracted (green). (e)–(h) $V^\star$ maps acquired at $z = 12.0$, 10.1, 9.8, and 9.6 Å. The experimental data in (h) is partially overlaid with models to indicate the position of individual atoms. All scale bars are 5 Å.

Figures 1(a) and 1(c) show the chemical structure and a Δf image of both molecules, respectively. To map out the local contact potential difference between the CO-functionalized tip and the sample, KPFS spectra [11] have been acquired on a dense grid of sample points over the molecules [4]. Each KPFS spectrum $\Delta f(V)$ shows a parabolic shape [see Fig. 1(d)] and from a fit to a parabola, the voltage $V^\star$, at which $\Delta f(V)$ has its maximum, is extracted. Usually, $V^\star$ is assumed to equal the voltage of compensated LCPD, such that $V_{\mathrm{LCPD}} = V^\star$ [11]. Figures 1(e)–1(f) show the maps of $V^\star$ values with decreasing tip-sample distance. For relatively large distances of 12.0 Å, these $V^\star$ maps show a contrast that is expected from an interface dipole formation [15]. For the remainder, it is important that any charge at the surface of the metal substrate will be screened efficiently (the image-charge effect) leading to a dipole rather than an isolated point charge [30]. Because of this and the superposition principle, any distribution of charges at a metal surface can equally be described by a set of dipoles, each perpendicular to the surface; see the inset in Fig. 2(a). Each of these dipoles will change the LCPD. This highlights the direct link between charges inside the adsorbate, the resulting surface dipoles, and LCPD. Upon approaching the surface slightly, Fig. 1(f), the $V^\star$ contrast increases and shows higher lateral resolution. The largest shifts of the $V^\star$ signal are observed at the circumference of the molecule. In agreement with this observation, our DFT simulations reveal that the interface dipoles at the two molecules of $-1.16D$ and $+3.87D$, respectively, are mainly due to vertical relaxations of the polar peripheral bonds of opposite polarity ($C^{\delta+} - F^{\delta-}$ vs $C^{\delta-} - H^{\delta+}$); see Fig. S5 in Ref. [22]. At the closest distance in the experiment, Fig. 1(h), mercury atoms within $F_{12}C_{18}Hg_3$ become apparent. In addition, the contrast inverses at the outer part of the phenylene groups, where it shows sharp red to blue transitions. Although this intramolecular contrast is remarkable, such a contrast inversion [10] is incompatible with the simple interpretation in terms of LCPD [22].

One possible contribution to the KPFS signal at close distances is the so-called phantom force [32] resulting from the current. However, a strong influence of phantom force can be excluded here, because (i) the tunneling current image [Fig. 1(b)] bears no resemblance to the features of the contrast inversion, and (ii) the tunneling current is similar for both molecules, whereas $V^\star$ is strikingly different.

Instead, it has been speculated that the contrast inversion stems from the probe penetrating the molecule's electron shell so that the unscreened core charges contribute to the KPFS signal [10]. Electrostatic force contributions give rise to the parabolic dependence of $\Delta f(V)$ [11,15]. From the above reasoning, no deviation from a parabolic shape is expected. Therefore, we analyzed the residuals of the parabolic fit to the KPFS spectra for different distances, as is shown in Fig. 2(b). Whereas, at large distances, the residuum is a random noise signal—it shows structure not compatible with noise at close distances. This systematic deviation from a parabolic shape points toward a contribution to the signal involving not only electrostatics.

The large electric fields in the junction on the order of 10^9 V/m that occur upon acquisition of a KPFS parabola will lead to a relaxation of the positions of atoms that carry net charge (ionic polarization), and a Stark effect of the electron shell (electronic polarization). Both effects will affect the overlap of the electron shells of tip and sample, contributing to the Pauli repulsion and hence to Δf in the close-distance regime [33]. As the Pauli repulsion is very short range in nature, even tiny relaxations lead to an appreciable signal. The above considerations provide a good reason why KPFS fails to reproduce LCPD in this regime. Upon sweeping the bias voltage, the sample and the tip will undergo relaxations affecting the Pauli repulsion and hence the frequency shift. Since this involves non-electrostatic interactions, a deviation from a parabolic shape of $\Delta f(V)$ can be expected. Even if this deviation is not immediately apparent from looking at the data, the fit of $V^\star$ might be heavily affected. To analyze this, we

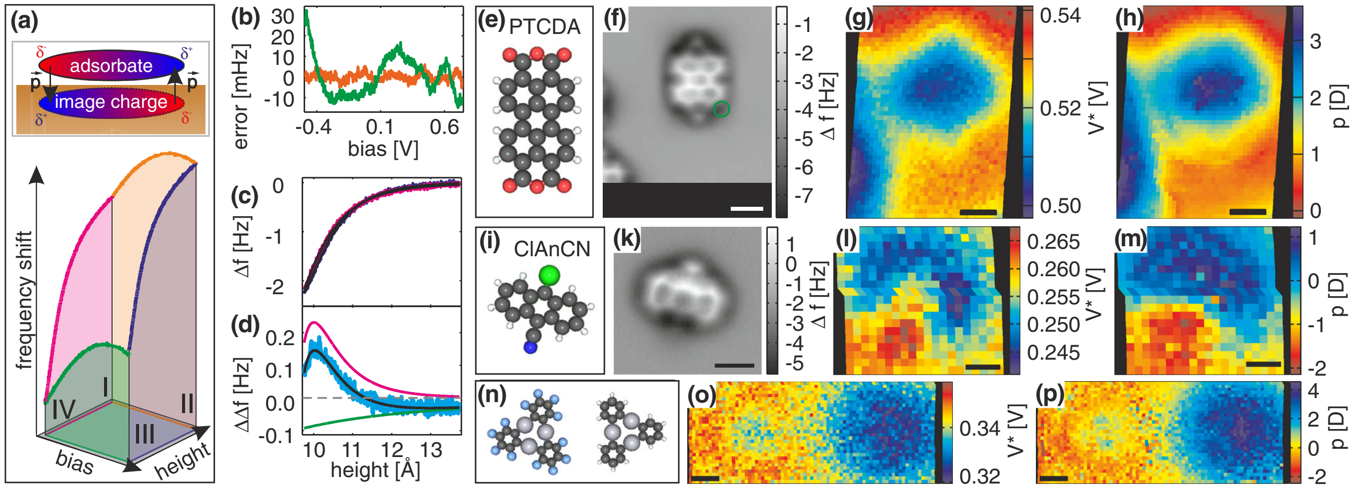

FIG. 2 (color online). Deducing intramolecular charge distribution from z ramps. (a) Schematic illustration of the data acquisition procedure: For each lateral grid position, two KPFS parabolas at different distances (I → II and III → IV) and two $\Delta f(z)$ curves at different voltages (II → III and IV → I) are recorded. (b) Residuals of the parabolic fit to KPFS data show just random noise for a large tip-sample spacing (orange) but systematic deviations for a short one (green). (Data points smoothed over 75 mV.) (c) Background subtracted $\Delta f(z, V_i)$ curves along with their Lennard-Jones fits. (d) The difference spectrum $\Delta\Delta f(z, \Delta V)$ (blue) is fitted by contributions from electrostatics (green) and vertical relaxation (pink), the sum of which is shown in black (the dashed gray line indicates zero). The green marker in (f) indicates the lateral position of the spectra shown in (a)–(d). (e)–(p) Comparison of dipole-distribution maps extracted from $\Delta f(z, V_i)$ spectra [(h), (m), (p)] and conventional KPFS maps [(g), (l), (o)] at relatively large distances for PTCDA [(e)–(h)], ClAnCN [(i)–(m)], and $F_{12}C_{18}Hg_3$ and $H_{12}C_{18}Hg_3$ [(n)–(p)] [31].

evaluated the goodness of the parabolic fit to the experimental $\Delta f(V)$ spectrum for each pixel of Fig. 1(h), revealing that the contrast inversion is spatially correlated with systematic deviations from parabolas; see Fig. S1 in Ref. [22].

Whereas the above considerations hint toward a fundamental limitation of KPFS to reproduce LCPD at very close distances, they offer a route to overcome the limitations of KPFS in charge detection at very close distances, as follows. The basic idea of the novel scheme is to better disentangle electrostatic from nonelectrostatic contributions of Δf from their different distance dependence [34]. In addition to KPFS spectra $\Delta f(V)$ (at a given tip height), we acquired $\Delta f(z)$ data for two distinctly different bias voltages V_i; see the schematic in Fig. 2(a). Both of these $\Delta f(z)$ curves are expected to display the distance dependence of the forces (or—more precisely—the tip-sample stiffness $\partial F_z/\partial z$) between tip and sample molecule. The interactions other than electrostatic in origin can be modeled by a Lennard-Jones potential; we therefore refer to the part of the $\Delta f(z)$ signal resulting from these contributions as $\Delta f_{\mathrm{LJ}}(z)$. A vertical relaxation δz resulting from the drastic change of bias voltage will—in good approximation [22]—simply shift the two $\Delta f(z)$ curves with respect to the vertical position z, so that $\Delta f_{\mathrm{LJ}}(z, V_2) \simeq \Delta f_{\mathrm{LJ}}(z + \delta z, V_1)$. As these relaxations are expected to be small, a Taylor expansion yields that the difference $\Delta f_{\mathrm{LJ}}(z,V_2) - \Delta f_{\mathrm{LJ}}(z,V_1) \simeq \Delta f_{\mathrm{LJ}}(z+\delta z,V_1) - \Delta f_{\mathrm{LJ}}(z,V_1) \simeq \delta z \cdot \Delta f'_{\mathrm{LJ}}(z,V_1)$ equals the product of δz times the derivative $\Delta f'_{\mathrm{LJ}}(z, V_1) = \partial \Delta f_{\mathrm{LJ}}(z, V_1)/\partial z$. Hence, the extraction of the difference signal may directly provide information about the polarization of molecules on surfaces.

Moreover, the two $\Delta f(z)$ spectra will also contain several electrostatic contributions which can be classified [35,36] in the ones that stem from the overall electrostatic tip-substrate interaction and those from local charges in the junction. The former can be eliminated by subtracting the $\Delta f(z)$ signal acquired away from the molecule on the bare substrate from each of the spectra at the given voltage. Henceforth, $\Delta f(z)$ refers to the background subtracted signal. Note that this background subtraction will not affect the considerations discussed in the previous paragraph. What remains are the contributions from local charges inside the junction. We make use of the fact that in the presence of the metal, they can be described by a set of vertical dipoles (see above). Each of these dipoles interacts with a local electric field in the junction. Even though the electric field is enhanced locally right beneath the tip [see Fig. S7 in Ref. [22]], we approximate it for simplicity as $(V_{\mathrm{bias}} - \mathrm{LCPD})/z$, where z is the tip-substrate distance [37].

As the surface dipole p and the electric field right beneath the functionalized tip are both oriented perpendicular to the surface, their interaction potential equals $p(V_{\mathrm{bias}} - \mathrm{LCPD})/z$. Differentiating this expression twice yields a corresponding $\Delta f(z)$ contribution, which is proportional to $p(V_{\mathrm{bias}} - \mathrm{LCPD})/z^3$. Hence, the difference spectrum $\Delta\Delta f(z, \Delta V) = \Delta f(z, V_2) - \Delta f(z, V_1)$ is expected to show two contributions: one being proportional to $\delta z \Delta f'(z, V_1)$ [due to vertical relaxation δz, the pink curve in Fig. 2(d)] and a second one proportional to $p\Delta V/z^3$ (the green curve) indicating the presence of surface dipoles p in the junction [38]. Note that the functional dependences on z of these two contributions are qualitatively different from each other and therefore allow one to discriminate between the two in a fitting procedure [39]. One has to be aware that the above proposed novel method and fitting procedure involve quite some simplifications and approximations [22].

Although we believe that extracting the bias-dependent vertical relaxation δz from these fits may turn out to be useful in the future, in the current experiment we attribute any such relaxations mainly to the CO at the tip [33] rather than to the molecule on the surface. We therefore disregard the relaxation δz and concentrate on the dipole maps only. Figure 2 displays the experiments following the scheme described above. For each point on a dense grid, we recorded the frequency shift as a function of the tip-sample spacing at two different bias voltages, as is exemplarily displayed for one individual grid point in a 3D representation in Fig. 2(a). The two spectra $\Delta f(z, V_1)$ and $\Delta f(z, V_2)$ are depicted in Fig. 2(c). Despite their similarity, the difference signal $\Delta\Delta f(z, \Delta V)$ displayed in Fig. 2(d) still shows distinct features. A comparison to the derivative $\Delta f'(z, V_1)$ (pink) shows striking agreement in the overall shape, which we view as a confirmation of the relaxation effect, as described above. The offset between the experimental data and $\Delta f'(z, V_1)$ indicates clearly that another contribution is missing. An additional contribution proportional to $-\Delta V/z^3$ (green) results in a sum (black) that excellently fits the data. From this fitting procedure, the dipole p is extracted for each grid point, rendering maps, which are henceforth referred to as dipole maps. To test the novel method, we compared such dipole maps to maps of $V^\star = V_{\mathrm{LCPD}}$ from KPFS at distances at which KPFS works reliably. The resulting maps are displayed in Figs. 2(e)–2(p) for PTCDA on copper, ClAnCN on the NaCl bilayer on copper, and for $F_{12}C_{18}Hg_3$ and $H_{12}C_{18}Hg_3$ on copper, along with a model of their chemical structure and a Δf image. In the case of ClAnCN, the NaCl bilayer was introduced to benchmark the method also for a distinctly different electronic coupling and current regime. In all cases the dipole maps [Figs. 2(h), 2(m), and 2(p)] closely resemble the $V^\star$ maps [cf. Figs. 2(g), 2(l), and 2(o)]. In turn, in this regime $V^\star$ maps are assumed to reflect the local charge distribution [4,10,15].

Lateral resolution and contrast increase drastically when the tip-sample spacing is reduced. A corresponding dipole map for $F_{12}C_{18}Hg_3$ and $H_{12}C_{18}Hg_3$ on copper is displayed in Fig. 3, along with a Δf image and the DFT calculated charge distribution, for comparison. Note that the dipole maps are expected to be a convolution of the local dipoles with the lateral profile of the electric field beneath the tip [40], smearing out the apparent dipole distribution. Remarkably, this map still shows pronounced intramolecular contrast without suffering from similar artifacts as the KPFS-derived map shown in Fig. 1(h). Interestingly, at the positions of the mercury atoms, the contrast in this map is much stronger than in the Δf images [cf. Figs. 1(c) and 3(a)].

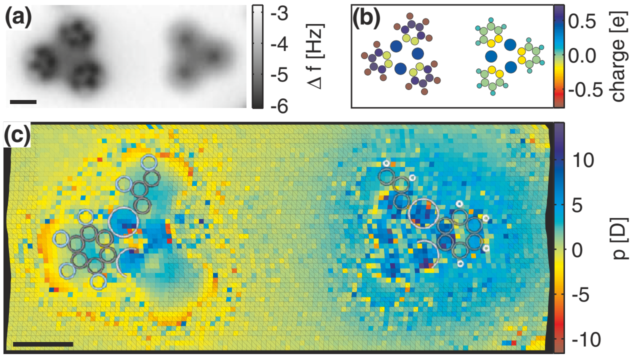

FIG. 3 (color online). Highly resolved dipole-distribution map. (a) Δf image recorded at $z = 9.6$ Å. (b) Calculated charge distribution deduced from Bader analysis. (For details, see Table S1 in Ref. [22].) (c) Dipole-distribution map extracted from $\Delta f(z, V_i)$ spectra for $F_{12}C_{18}Hg_3$ and $H_{12}C_{18}Hg_3$ (9.6 Å $\leq z \leq$ 10.1 Å; $V_i = -0.2$ and 0.5 V).

The dipole map shows a contrast that is in agreement with the calculated charge distribution [see Fig. 3(b)] and the electrostatic potential map (see Ref. [22]). The contrast observed at the circumference of the molecules fits to the overall surface dipole as discussed above. Directly along the C-F bonds a strong contrast change from green to red indicates the electrons being pulled toward the fluorine ($C^{\delta+} - F^{\delta-}$). The C-H bonds show much less of a polar nature, with a tendency toward $C^{\delta-} - H^{\delta+}$ in accordance with the Bader analysis [see Fig. 3(b)]. The map also reveals that the mercury atoms on both molecules apparently carry net positive charge, in good agreement with DFT. The signal on benzene rings shows relatively weak contrast with respect to Hg atoms, in fair agreement with the calculations.

It needs to be emphasized that the dipole maps—even though provided in units of Debye—may not be taken as being quantitative. Experimental uncertainties in determining the absolute tip-sample distance, averaging effects, the bending of the CO molecule at the tip apex, the approximations made in the fitting procedure, and tip-induced surface dipoles may influence the quantitative interpretation. Nonetheless, we are convinced that this novel technique presents a route to better disentangle electrostatic from nonelectrostatic contributions to overcome the limitations of KPFS at closest distances and highest resolution. It may even be a first step toward a quantitative determination of surface dipoles.

In conclusion, the experiments presented here provide insight as to why KPFS systematically fails to reproduce the LPCD at very close tip-sample distances. We introduce a new method that allows for resolving intramolecular charge distributions with unprecedented resolution, showing contrast at the atomic scale.

We thank Andreas Pöllmann, François P. Gabbaï, John McManus, Leo Gross, Niko Pavliček, Norio Okabayashi, Pingo Mutombo, and Prokop Hapala for the fruitful discussions and the help. We greatly appreciate the support from the National Grid Infrastructure MetaCentrum (Project No. LM2010005) for our calculations. We are grateful for funding by the DFG and the GAČR (through Research Training Group 1570 and Grand No. Sche 384/26-2 and the German-Czech bilateral Project Nos. RE2669/4; 14-16963J) and the Volkswagen foundation (through its "Lichtenberg" program).

---

[*]Corresponding author.
Jascha.Repp@ur.de

[1] L. Gross, F. Mohn, N. Moll, P. Liljeroth, and G. Meyer, Science **325**, 1110 (2009).

[2] L. Gross, F. Mohn, N. Moll, G. Meyer, R. Ebel, W. M. Abdel-Mageed, and M. Jaspars, Nat. Chem. **2**, 821 (2010).

[3] Z. Sun, M. P. Boneschanscher, I. Swart, D. Vanmaekelbergh, and P. Liljeroth, Phys. Rev. Lett. **106**, 046104 (2011).

[4] F. Mohn, L. Gross, N. Moll, and G. Meyer, Nat. Nanotechnol. **7**, 227 (2012).

[5] N. Pavliček, B. Fleury, M. Neu, J. Niedenführ, C. Herranz-Lancho, M. Ruben, and J. Repp, Phys. Rev. Lett. **108**, 086101 (2012).

[6] J. Welker and F. J. Giessibl, Science **336**, 444 (2012).

[7] F. Albrecht, M. Neu, C. Quest, I. Swart, and J. Repp, J. Am. Chem. Soc. **135**, 9200 (2013).

[8] D. G. de Oteyza, P. Gorman, Y.-C. Chen, S. Wickenburg, A. Riss, D. J. Mowbray, G. Etkin, Z. Pedramrazi, H.-Z. Tsai, A. Rubio, M. F. Crommie, and F. R. Fischer, Science **340**, 1434 (2013).

[9] J. van der Lit, M. P. Boneschanscher, D. Vanmaekelbergh, M. Ijäs, A. Uppstu, M. Ervasti, A. Harju, P. Liljeroth, and I. Swart, Nat. Commun. **4**, 2023 (2013).

[10] B. Schuler, S.-X. Liu, Y. Geng, S. Decurtins, G. Meyer, and L. Gross, Nano Lett. **14**, 3342 (2014).

[11] M. Nonnenmacher, M. P. O'Boyle, and H. K. Wickramasinghe, Appl. Phys. Lett. **58**, 2921 (1991).

[12] R. Bennewitz, M. Bammerlin, M. Guggisberg, C. Loppacher, A. Baratoff, E. Meyer, and H.-J. Güntherodt, Surf. Interface Anal. **27**, 462 (1999).

[13] S. A. Burke, J. M. LeDue, Y. Miyahara, J. M. Topple, S. Fostner, and P. Grütter, Nanotechnology **20**, 264012 (2009).

[14] S. Sadewasser, P. Jelinek, C.-K. Fang, O. Custance, Y. Yamada, Y. Sugimoto, M. Abe, and S. Morita, Phys. Rev. Lett. **103**, 266103 (2009).

[15] J. L. Neff and P. Rahe, Phys. Rev. B **91**, 085424 (2015).

[16] R. Stomp, Y. Miyahara, S. Schaer, Q. Sun, H. Guo, P. Grutter, S. Studenikin, P. Poole, and A. Sachrajda, Phys. Rev. Lett. **94**, 056802 (2005).

[17] L. Gross, F. Mohn, P. Liljeroth, J. Repp, F. J. Giessibl, and G. Meyer, Science **324**, 1428 (2009).

[18] T. Leoni, O. Guillermet, H. Walch, V. Langlais, A. Scheuermann, J. Bonvoisin, and S. Gauthier, Phys. Rev. Lett. **106**, 216103 (2011).

[19] F. J. Giessibl, Appl. Phys. Lett. **76**, 1470 (2000).

[20] T. R. Albrecht, P. Grütter, D. Horne, and D. Rugar, J. Appl. Phys. **69**, 668 (1991).

[21] G. Kresse and J. Furthmüller, Phys. Rev. B **54**, 11169 (1996).

[22] See Supplemental Material at http://link.aps.org/supplemental/10.1103/PhysRevLett.115.076101, which includes Refs. [23–29], for details on methods and approximations used and for additional results of both measurement and calculations.

[23] U. Dürig, H. R. Steinauer, and N. Blanc, J. Appl. Phys. **82**, 3641 (1997).

[24] P. Sartori and A. Golloch, Chem. Ber. **101**, 2004 (1968).

[25] G. Wittig and F. Bickelhaupt, Chem. Ber. **91**, 883 (1958).

[26] T. J. Taylor, C. N. Burress, and F. P. Gabbaï, Organometallics **26**, 5252 (2007).

[27] D. Vanderbilt, Phys. Rev. B **41**, 7892 (1990).

[28] J. P. Perdew, J. A. Chevary, S. H. Vosko, K. A. Jackson, M. R. Pederson, D. J. Singh, and C. Fiolhais, Phys. Rev. B **48**, 4978 (1993).

[29] G. Henkelman, A. Arnaldsson, and H. Jónsson, Comput. Mater. Sci. **36**, 354 (2006).

[30] J. D. Jackson, *Classical Electrodynamics* (Wiley, New York, 2001).

[31] Tip heights for PTCDA: Δf image 9.0 Å, $V^\star$ map 12.6 Å, charge map z sweep between 12.6 and 9.6 Å at −0.4 and 0.75 V bias. Tip heights for ClAnCN: Δf image at 15.4 Å, $V^\star$ map at 18.2 Å, charge map z sweep between 18.2 and 16.2 Å at −0.5 and 0.5 V bias. Tip heights for $F_{12}C_{18}Hg_3$ and $H_{12}C_{18}Hg_3$: $V^\star$ map at 11.0 Å, charge map z sweep between 11.5 and 9.9 Å at −0.2 and 0.35 V bias.

[32] A. J. Weymouth, T. Wutscher, J. Welker, T. Hofmann, and F. J. Giessibl, Phys. Rev. Lett. **106**, 226801 (2011).

[33] N. Moll, L. Gross, F. Mohn, A. Curioni, and G. Meyer, New J. Phys. **14**, 083023 (2012).

[34] M. A. Lantz, H. J. Hug, R. Hoffmann, P. J. A. van Schendel, P. Kappenberger, S. Martin, A. Baratoff, and H.-J. Güntherodt, Science **291**, 2580 (2001).

[35] L. Gross, B. Schuler, F. Mohn, N. Moll, N. Pavliček, W. Steurer, I. Scivetti, K. Kotsis, M. Persson, and G. Meyer, Phys. Rev. B **90**, 155455 (2014).

[36] A. Sadeghi, A. Baratoff, S. A. Ghasemi, S. Goedecker, T. Glatzel, S. Kawai, and E. Meyer, Phys. Rev. B **86**, 075407 (2012).

[37] Note that the dipole under consideration is in direct proximity to the sample, where this approximation is justified. For an estimate of the vertical tip-sample distance, see Ref. [22].

[38] For the conversion factor to extract the dipole in physically meaningful units, see Ref. [22].

[39] Changing the exponents of the Lennard-Jones fit from a (12-6) potential to a (12-4) potential did not affect the fit result for the dipole maps qualitatively.

[40] D. Z. Gao, J. Grenz, M. B. Watkins, F. Federici Canova, A. Schwarz, R. Wiesendanger, and A. L. Shluger, ACS Nano **8**, 5339 (2014).

Charge Redistribution and Transport in Molecular Contacts

Martina Corso,[1,2,3,*] Martin Ondráček,[4] Christian Lotze,[1] Prokop Hapala,[4]
Katharina J. Franke,[1] Pavel Jelínek,[4] and J. Ignacio Pascual[1,3,5]
[1]*Institut für Experimentalphysik, Freie Universität Berlin, 14195 Berlin, Germany*
[2]*Centro de Fisica de Materiales CSIC/UPV-EHU, 20018 Donostia-San Sebastian, Spain*
[3]*Ikerbasque, Basque Foundation for Science, 48011 Bilbao, Spain*
[4]*Institute of Physics of the Academy of Sciences of the Czech Republic, 162 00 Prague, Czech Republic*
[5]*CIC nanoGUNE, 20018 Donostia-San Sebastian, Spain*

(Received 18 March 2015; revised manuscript received 8 July 2015; published 22 September 2015)

The forces between two single molecules brought into contact, and their connection with charge transport through the molecular junction, are studied here using non contact AFM, STM, and density functional theory simulations. A carbon monoxide molecule approaching an acetylene molecule (C_2H_2) initially feels weak attractive electrostatic forces, partly arising from charge reorganization in the presence of molecular . We find that the molecular contact is chemically passive, and protects the electron tunneling barrier from collapsing, even in the limit of repulsive forces. However, we find subtle conductance and force variations at different contacting sites along the C_2H_2 molecule attributed to a weak overlap of their respective frontier orbitals.

DOI: 10.1103/PhysRevLett.115.136101 PACS numbers: 68.37.Ps, 34.20.Gj, 73.63.Rt, 74.55.+v

The formation of an atomic-sized contact between two solids is an intriguing problem in physics [1]. Basic properties of nanoscale solids and composite materials, such as adhesion, friction, or electrical conductance, depend on the nature of their contacts at the atomic level. At proximity length scales comparable to the atomic dimensions and the electronic Fermi wavelength, the onset of electrical and a mechanical contact can be independently defined and may occur at different atomic separations [2]. For example, electronic transport through atomic contacts in metals is ballistic before the mechanical contact (i.e., bond equilibrium position) because the strong hybridization of localized atomic orbitals precedes the point of mechanical stability [3]. Atomic-scale contacts may also endow the system with new properties. In covalent contacts between semiconductors or molecular radicals, the hybridization of frontier orbitals may be accompanied by a strong redistribution of charges creating electrostatic barriers [4] or reducing the conductance of the contact [5,6].

In contrast, the contact between (close-shell) molecules is weak and stabilized by van der Waals interactions. Thus, it has a larger bond equilibrium distance, and the electrical conduction decreases due to smaller wave-function overlap [7]. The weak intermolecular forces are, however, highly sensitive to small changes of their surrounding electrostatic landscape and to structural rearrangements [7,8]. This is a key concept behind the electronic functionality of soft organic materials because charge hopping and electronic delocalization are determined by the overlap of the molecular orbitals [9].

In this Letter, we study the correlation of electrical transport and short-range forces during the formation of a weak contact between two molecules using simultaneous force and current measurements in a scanning tunneling microscope. To create a robust molecular junction, we use carbon monoxide (CO) functionalized tips. These have shown to be stable at very short distances. Numerous studies resolved the chemical structure of adsorbed molecules with atomic and bond resolution [10–16] at the onset of Pauli repulsion forces. As counter electrode, we used an acetylene molecule (C_2H_2) on a copper substrate. We find that weak attractive forces are enhanced by the formation of dipoles induced by the charge reorganization due to the proximity of the molecules. The interaction landscape is further correlated with the tunneling transmission of the junction. The two molecules behave as chemically passive spacers, with low transmission tunneling channels even when compressive forces are applied. However, contacting the acetylene at the C═C bond leads to relatively larger electrical transmission, confirming that electrical properties of organic systems are very sensitive to details on their structure.

We used a combined STM/non contact AFM based on a qPlus sensor design [17] operated in frequency modulation mode [18], at 5 K and in ultrahigh vacuum [19]. We measured frequency shift $\Delta f(x,z)$ plots, and determined the corresponding vertical force $F_z(x,z)$ in the pN range using the Sader and Jarvis method [20]. To provide quantitative values of forces and energies between the molecules, we removed the $\Delta f(x,z)$ background due to long-range forces between the metal tip and sample [21] [see Supplemental Material [22]]. For simultaneous conductance measurements $G(x,z)$, a small bias of 80 mV was applied [22].

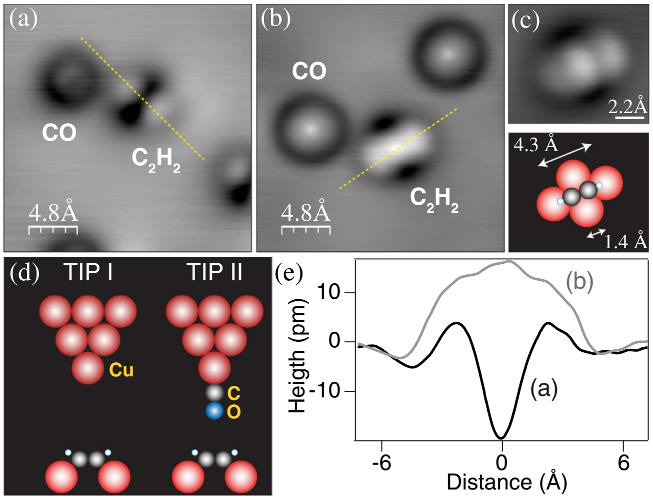

FIG. 1 (color online). (a), (b) Constant current STM images taken on CO and C_2H_2 molecules in different sample positions at $V = 100$ mV and $I = 0.15$ nA. These images [(a) and (b)] were measured, respectively, with the tip terminations schematically drawn in (d): a sharp Cu tip (I) and a CO tip (II). The appearance of a C_2H_2 with a CO tip and its adsorption geometry from [28] are shown in (c). (e) Topography profiles taken along the yellow lines measured on the C_2H_2 in (a) and (b).

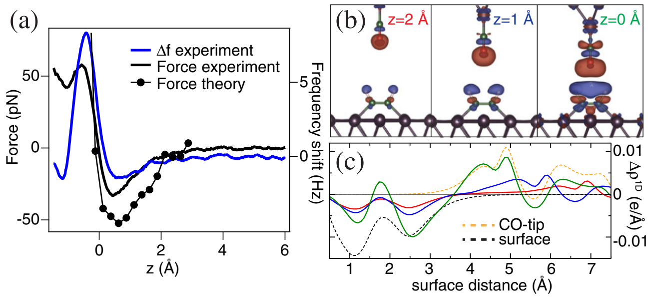

FIG. 2 (color online). (a) Frequency shift (Δf) and the corresponding vertical force [20] measured with a CO functionalized tip at $V = 0$ mV as a function of the tip-sample distance (z) over the C═C bond of a C_2H_2 molecule (further details in [22]). Δf is corrected for the macroscopic influence of the tip as explained in [22]. The calculated force is included as dots for comparison. (b) Development of the induced electron density $\Delta\rho = \rho_{\text{tot}} - \rho_{\text{surf}} - \rho_{\text{tip}}$ and (c) its projection into z, $\Delta\rho^{1D} = \int\int \Delta\rho dxdy$ at three CO-acetylene distances. In (b), we plot $\Delta\rho$ isosurfaces at 0.0005 e/Å, where blue and red mean depletion and accumulation of electrons, respectively. Dashed black and yellow lines in (c) show induced electron density of noninteracting free standing acetylene-surface and CO tip, when an electric field 0.1 eV/Å is applied.

Acetylene molecules were deposited on a clean Cu(111) surface at 130 K, together with a small amount of CO molecules for functionalizing the tip apex. On the Cu(111) surface, acetylene undergoes a strong hybridization which converts the central sp bond into a double bond and bends the hydrogen atoms upwards [see Fig. 1(d)] [28]. We transferred a CO molecule to the apex of the STM tip as described in Ref. [29]. In most cases, the CO molecule adopts a standing up configuration on the tip apex, exposing the oxygen atom outwards [Fig. 1(d)] [30].

The shape of acetylene in the STM images varies depending on the termination of the tip apex. Figure 1 compares constant current STM images obtained with a sharp copper tip (a) and with a CO-functionalized tip (b) and (c). In the first case [Fig. 1(a)], acetylene is imaged with a characteristic dumbbell shape [31,32]. Using a CO functionalized tip, the contrast of acetylene is reversed, and appears with a three lobed structure peaked by a central maximum, clearly visible in the line profile in Fig. 1(e). This is due to the symmetry enhanced tunneling contribution from CO p orbitals into π^* states of acetylene [33].

Electrostatic origin of short range forces.—First, we address the identification of the interaction forces between CO and acetylene molecules in close proximity. Figure 2 shows the frequency shift (Δf) and the integrated force as a function of their separation z [22]. Both molecules attract each other in a short distance range of ∼2 Å and form a stable bond at $z = 0$ Å. We defined this point (z_0) as the distance where short-range forces are relaxed [$F_z(z_0)$], i.e., the energy minimum or equilibrium bond distance. The maximum attractive force before that point reaches 33 ± 5 pN. The bond created between the two species is clearly noncovalent, with binding energy of -70 ± 5 meV [22].

Repulsive (Pauli) forces build up in the junction, when approaching the tip, to closer positions. In this region, a characteristic maxima in Δf can be observed, which gives rise to a small relaxation of forces at the junction [22]. As we shall show below, such relaxation can be attributed to the bending of the CO molecule at the tip.

To unveil the origin of the attractive molecular forces, we performed density functional theory (DFT)-based simulations of the interaction between the two molecules adsorbed in their respective environment (details are given in the Supplemental Material [22]). The force simulations reproduce well the results of the AFM measurement [Fig. 2(a)], obtaining a maximal attractive force of 52 pN over the center of the C_2H_2 molecule. The force minimum is reached at a distance of 75 pm (50 pm in the experiment) before a relaxed bond is formed ($F_z = 0$ point); thus, it is a short range force. This force has two main components. A fraction of it is due to molecular London dispersion forces, amounting to 27.5 pN. The rest is due to electrostatic forces related to static dipoles and to the charge redistribution induced by the proximity of the molecules.

The origin of this last attractive force component can be tracked down by analyzing the induced charge density ($\Delta\rho$) due to the interaction between CO and C_2H_2 molecules. Figure 2(b) shows $\Delta\rho$ isosurfaces at three different CO-C_2H_2 separations, from the onset of attractive forces ($z = 2$ Å) to the point of minimum energy, z_0. We observe, in all the cases, no trace of electron accumulation in the CO-C_2H_2 gap, supporting the absence of the covalent character of the bond between the two molecules. However, there is a growing charge redistribution as the molecules approach, leading to increasing polarization of the opposite sign of both CO and C_2H_2, and explaining the build up of attractive, short-range electrostatic forces.

The charge rearrangement in the absence of wave-function overlap is due to the existence of a finite dipole moment of the molecules [34], and their effect on the local work functions of tip and sample: the CO molecule increases the copper work function, whereas C_2H_2 decreases it [22]. The result is the existence of a finite electric field E_{loc} at the tunneling junction, which increases and enhances the electrical polarization of the molecules as they are approached. In fact, by applying a homogeneous electric field of $E_z = 0.1$ eV/Å to either the CO-tip or C_2H_2 sample, we obtain a similar charge redistribution as when the tip is at z_0 [see dashed lines in $\Delta\rho$ plots of Fig. 2(c)]. The electrostatic field E_{loc} built up at the junction causes variations of the local contact potential difference with the tip-sample separation, which are crucial for interpreting local Kelvin probe force spectroscopy measurements [4,35,36].

Correlation of forces with charge transport.—The absence of covalent character at the CO-C_2H_2 bond implies that a tunneling mechanism may be required to describe the charge transport across the junction. Therefore, the electrical conductance is expected to be low but very sensitive to small forces affecting the molecular junction. To obtain the conductance of a relaxed CO-C_2H_2 molecular junction, we measured, simultaneously, the linear conductance (G) and Δf as a CO tip was approached at different sites along an acetylene molecule. The resulting $G(x, z)$ and $F_z(x, z)$ maps are shown in Fig. 3. The $G(x, z)$ map corroborates that the conductance over the C═C bond of acetylene is the largest along the molecule [33,38]. The profile of bond equilibrium distance $z_0(x)$ [white contour in Fig. 3(b)] shows a minimum at the C═C bond, reflecting that, at the center, forces have a shorter range (and are more attractive than over the H atoms [22]) probably due to the H atoms bending upwards. In the inset of Fig. 3(b), we plot the conductance values at the $z_0(x)$ positions. The conductance of a CO molecule bonding to the C═C site of acetylene turns out to be a factor of 2 larger than when contacting the hydrogen atoms.

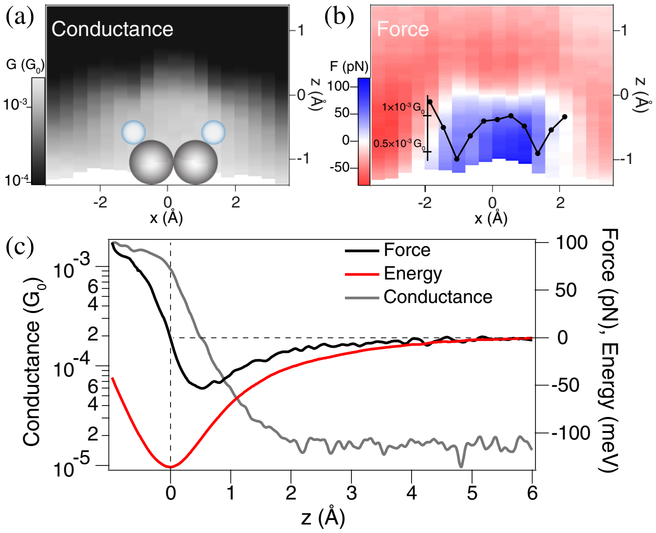

FIG. 3 (color online). (a), (b) Conductance and force maps recorded simultaneously along a C_2H_2 molecular axis while applying a bias of $V = 80$ mV to the sample. Similar force maps are obtained at zero bias [22]. The plot in (b) shows the value of the conductance at zero force. G is plotted in logarithmic scale in units of the quantum of conductance $G_0 = 2e^2/h = (12\,906\ \Omega)^{-1}$. Both force and conductance are obtained after deconvolution of the tip oscillation [20,37]. (c) Conductance, force, and energy curves taken at the C═C bond with a CO tip. A change in conductance occurs at the energy minimum.

The measured tunneling conductance at the $F_z(z_0) = 0$ turning point amounts to $\sim 10^{-3} G_0$ $(G_0 = e^2/\pi\hbar)$ [Figs. 3(b) and 3(c)]. This low value confirms the persistence of a tunneling barrier at this contact point. In Fig. 4(a), we show the Hartree potential (the electrostatic potential felt by electrons) calculated in the gap between the CO at the tip and the C_2H_2 molecule. The tunneling barrier does not collapse during the approach, and remains substantially above the Fermi level even when the force turning point z_0 is reached and forces become repulsive. The calculated conductance is in all the process far below one quantum of conductance. This behavior is, thus, a characteristic of the noncovalent character of the bond, and contrasts with the case of metallic atomic contacts, where the tunneling barrier was found to collapse in contact [3], and the transport becomes ballistic.

Bending of the CO molecule.—Compressing the molecular junction into the repulsive regime leads to a change of slope in the $G(z)$ plot [Fig. 3(c)] which resembles the transition to ballistic transport of metallic and molecular point contacts [39,40]. However, we note that this flattening coincides with an inflection also visible in the short-range $F - z$ force curve, and is responsible for the characteristic peak observed in the Δf plots of Fig. 2(a) and in [22]. Thus, the flattening of the $G(z)$ plot is a consequence of a mechanical rearrangement of the junction in order to relax repulsive forces [7]. The most probable change is the bending of the tip apex. It has been shown that a CO molecule on the apex can be easily tilted away from its original direction in response to lateral attractive forces [41,42]. In our case, sufficiently large repulsive forces in the junction (up to 50 pN, as seen in Fig. 2 and SOI) induce the lateral bending of the CO molecule [43] when approaching to potential saddle points such as the C═C bond. In this way, the CO molecule amplifies the response of the AFM to a potential landscape. This mechanism has been identified as responsible for intra-, and intermolecular bond contrast in constant height AFM images [44–47].

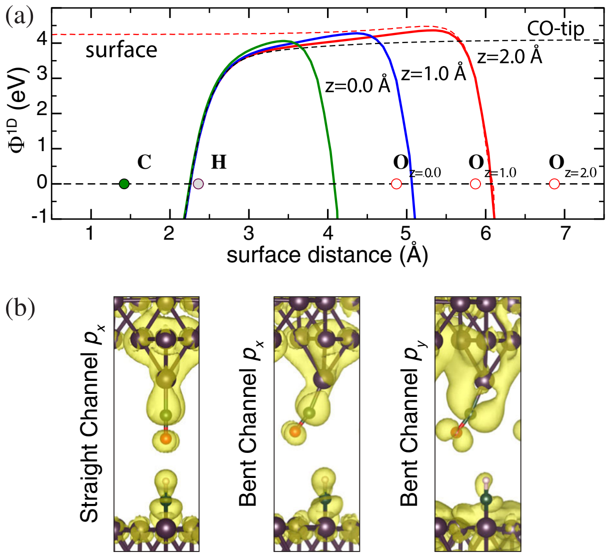

FIG. 4 (color online). (a) Development of the electrostatic (Hartree) potential felt by electrons in the gap between the tip and the acetylene molecule on the surface as the tip gradually approaches to the surface. The potentials are plotted along the CO molecular axis. Dashed black and red lines plot the electrostatic potential of the free standing surface and CO tip, respectively. The position of individual atoms of the acetylene molecule on the surface and oxygen atom on the tip at different tip-sample distances is schematically presented. All potentials are rendered with respect to the Fermi level. (b) Spatial distribution of the dominant eigenchannels at the Fermi energy for straight and bent CO configuration at the same tip-sample distance $z = 0$ Å.

The bending of the CO molecule affects the electron tunneling in two ways: First, it avoids the collapse of the tunneling barrier as the tip approaches. Second, it reduces the symmetry of the junction. To evaluate the impact of a reduced symmetry on tunneling, we calculated the transmission function of the different channels using nonequilibrium Green's function formalism implemented in the Smeagol code [48] together with the Fireball code [49]. Interestingly, the bending of the CO molecule over the C═C nodal plane leads to a swap of the leading transmission channels. For a straight CO tip, we find that the eigenchannel with p_x character is responsible for the majority of conductance (x direction along the C_2H_2 axis), in agreement with [33]. The bending of the CO tip drastically reduces the transmission through this channel, while another channel with prevailing p_y orbital character dominates the tunneling. For a straight CO molecule, this channel was not active in the charge transport because its nodal plane lies along the C_2H_2 axis. When the symmetry is reduced, one of its lobes couples with the C_2H_2 orbitals [Fig. 4(c)], allowing the flow of charge (see Section S3 in the Supplemental Material [22]). The consequence of the tip bending is, thus, a change of symmetry of the main tunneling channel, which should lead to a change in conductance contrast for short distances.

In summary, the short range interactions between a small hydrocarbon such as acetylene and a CO molecule at the tip of an AFM show a weak attractive component originating from their intrinsic dipole moment and from the charge redistribution upon chemisorption. The electrical polarization of the molecules rises as they are brought into contact, leading to a gradual increase in the contact potential difference. However, the two molecules are chemically passive, and no chemical bond was formed even when they enter in a regime of repulsive forces. The lack of chemical activity protects the tunneling barrier from collapsing and allows us to perform stable force and conductance mapping in the regime of repulsive forces. We found that repulsive forces cause the bending of the CO molecule and the decrease of the stiffness of the junction.

We thank Peter Saalfrank for discussions. The research was supported by DFG (Grant No. Sfb 658), the Czech Science Foundation (GAČR) Project No. 14-02079S, GAAV Grant No. M100101207, and the Spanish MINECO (Grant No. MAT2013-46593-C6-01). M. C. acknowledges support from the Alexander von Humboldt Foundation.

---

[*]Corresponding author.
martina.corso@ehu.eus

[1] N. Agrait, A. Levy-Yeyati, and J. M. van Ruitenbeek, Phys. Rep. **377**, 81 (2003).
[2] U. Dürig, O. Züger, and D. W. Pohl, Phys. Rev. Lett. **65**, 349 (1990).
[3] M. Ternes, C. González, C. P. Lutz, P. Hapala, F. J. Giessibl, P. Jelínek, and A. J. Heinrich, Phys. Rev. Lett. **106**, 016802 (2011).
[4] S. Sadewasser, P. Jelinek, C.-K. Fang, O. Custance, Y. Yamada, Y. Sugimoto, M. Abe, and S. Morita, Phys. Rev. Lett. **103**, 266103 (2009).
[5] P. Jelínek, M. Svec, P. Pou, R. Perez, and V. Cháb, Phys. Rev. Lett. **101**, 176101 (2008).
[6] A. Shiotari, Y. Kitaguchi, H. Okuyama, S. Hatta, and T. Aruga, Phys. Rev. Lett. **106**, 156104 (2011).
[7] A. Yazdani, D. M. Eigler, and N. D. Lang, Science **272**, 1921 (1996).
[8] N. Hauptmann, F. Mohn, L. Gross, G. Meyer, T. Frederiksen, and R. Berndt, New J. Phys. **14**, 073032 (2012).
[9] V. Coropceanu, J. Cornil, D. A. da Silva Filho, Y. Olivier, R. Silbey, and J. L. Brédas, Chem. Rev. **107**, 926 (2007).
[10] L. Gross, F. Mohn, N. Moll, P. Liljeroth, and G. Meyer, Science **325**, 1110 (2009).
[11] L. Gross, F. Mohn, N. Moll, G. Meyer, R. Ebel, W. Abdel-Mageed, and M. Jaspars, Nat. Chem. **2**, 821 (2010).
[12] F. Mohn, L. Gross, and G. Meyer, Appl. Phys. Lett. **99**, 053106 (2011).
[13] G. Kichin, C. Weiss, C. Wagner, S. Tauz, and R. Temirov, J. Am. Chem. Soc. **133**, 16847 (2011).
[14] N. Pavliček, B. Fleury, M. Neu, J. Niedenführ, C. Herranz-Lancho, M. Ruben, and J. Repp, Phys. Rev. Lett. **108**, 086101 (2012).

[15] D. G. de Oteyza, P. Gorman, Y.-C. Chen, S. Wickenburg, A. Riss, D. J. Mowbray, G. Etkin, Z. Pedramrazi, H.-Z. Tsai, A. Rubio, M. F. Crommie, and F. R. Fischer, Science **340**, 1434 (2013).

[16] A. Riss, S. Wickenburg, P. Gorman, L. Z. Tan, H.-Z. Tsai, D. G. de Oteyza, Y.-C. Chen, A. J. Bradley, M. M. Ugeda, G. Etkin, S. G. Louie, F. R. Fischer, and M. F. Crommie, Nano Lett. **14**, 2251 (2014).

[17] F. J. Giessibl, Appl. Phys. Lett. **76**, 1470 (2000).

[18] T. R. Albrecht, P. Grütter, D. Horne, and D. Rugar, J. Appl. Phys. **69**, 668 (1991).

[19] The qPlus sensor in this experiment is characterized by: a spring constant $k_0 \approx 1.8$ kN/m), resonance frequency of $f_0 = 20.7$ kHz, and quality factor $Q \approx 1.6 \times 10^4$. The data here presented are measured with a constant oscillation amplitude of $A_{\mathrm{osc}} \approx 30$ pm. The tip-sample distance is given as the vertical displacement from a reference position given by the set point parameters on the Cu substrate.

[20] J. E. Sader and S. P. Jarvis, Appl. Phys. Lett. **84**, 1801 (2004).

[21] Z. Sun, M. P. Boneschanscher, I. Swart, D. Vanmaekelbergh, and P. Liljeroth, Phys. Rev. Lett. **106**, 046104 (2011).

[22] See Supplemental Material at http://link.aps.org/supplemental/10.1103/PhysRevLett.115.136101 for details of the experimental and theoretical methods, the origin of short-range electrostatic interaction and an effect of the CO bending on the conductance, which includes Refs. [23–27].

[23] G. Kresse and J. Furthmüller, Phys. Rev. B **54**, 11169 (1996).

[24] D. Vanderbilt, Phys. Rev. B **41**, 7892 (1990).

[25] J. P. Perdew, J. A. Chevary, S. H. Vosko, K. A. Jackson, M. R. Pederson, D. J. Singh, and C. Fiolhais, Phys. Rev. B **46**, 6671 (1992).

[26] S. Grimme, J. Comput. Chem. **27**, 1787 (2006).

[27] M. Paulsson and M. Brandbyge, Phys. Rev. B **76**, 115117 (2007).

[28] W. Liu, J. S. Lian, and Q. Jiang, J. Phys. Chem. C **111**, 18189 (2007).

[29] L. Bartels, G. Meyer, and K.-H. Rieder, Appl. Phys. Lett. **71**, 213 (1997).

[30] S. Ishi, Y. Ohno, and B. Viswanathan, Surf. Sci. **161**, 349 (1985).

[31] B. C. Stipe, M. A. Rezaei, and W. Ho, Phys. Rev. Lett. **81**, 1263 (1998).

[32] Y. Konishi, Y. Sainoo, K. Kanazawa, S. Yoshida, A. Taninaka, O. Takeuchi, and H. Shigekawa, Phys. Rev. B **71**, 193410 (2005).

[33] L. Gross, N. Moll, F. Mohn, A. Curioni, G. Meyer, F. Hanke, and M. Persson, Phys. Rev. Lett. **107**, 086101 (2011).

[34] M. Schneiderbauer, M. Emmrich, A. J. Weymouth, and F. J. Giessibl, Phys. Rev. Lett. **112**, 166102 (2014).

[35] F. Mohn, L. Gross, N. Moll, and G. Meyer, Nat. Nanotechnol. **7**, 227 (2012).

[36] B. Schuler, S.-X. Liu, Y. Geng, S. Decurtins, G. Meyer, and L. Gross, Nano Lett. **14**, 3342 (2014).

[37] J. E. Sader and Y. Sugimoto, Appl. Phys. Lett. **97**, 043502 (2010).

[38] N. Pavliček, I. Swart, J. Niedenführ, G. Meyer, and J. Repp, Phys. Rev. Lett. **110**, 136101 (2013).

[39] N. Néel, J. Kröger, L. Limot, T. Frederiksen, M. Brandbyge, and R. Berndt, Phys. Rev. Lett. **98**, 065502 (2007).

[40] G. Schulze, K. J. Franke, A. Gagliardi, G. Romano, C. S. Lin, A. L. Rosa, T. A. Niehaus, Th. Frauenheim, A. Di Carlo, A. Pecchia, and J. I. Pascual, Phys. Rev. Lett. **100**, 136801 (2008).

[41] M. Neu, N. Moll, L. Gross, G. Meyer, F. J. Giessibl, and J. Repp, Phys. Rev. B **89**, 205407 (2014).

[42] A. J. Weymouth, T. Hofmann, and F. J. Giessibl, Science **343**, 1120 (2014).

[43] From our DFT simulations, we obtain that the CO molecule undergoes the larger structural relaxation (165 pm lateral relaxation), whereas the relaxation of all acetylene atoms is less than 3 pm.

[44] L. Gross, F. Mohn, N. Moll, B. Schuler, A. Criado, E. Guitián, D. Pea, A. Gourdon, and G. Meyer, Science **337**, 1326 (2012).

[45] A. M. Sweetman, S. P. Jarvis, H. Sang, I. Lekkas, P. Rahe, Y. Wang, J. Wang, N. R. Champness, L. Kantorovich, and P. Moriarty, Nat. Commun. **5**, 3931 (2014).

[46] P. Hapala, G. Kichin, C. Wagner, F. Stefan Tautz, R. Temirov, and P. Jelínek. Phys. Rev. B **90**, 085421 (2014).

[47] S. K. Hämäläinen, N. van der Heijden, J. van der Lit, S. den Hartog, P. Liljeroth, and I. Swart, Phys. Rev. Lett. **113**, 186102 (2014).

[48] A. R. Rocha, V. M. García-Suárez, S. Bailey, C. Lambert, J. Ferrer, and S. Sanvito, Phys. Rev. B **73**, 085414 (2006).

[49] J. P. Lewis *et al.*, Phys. Status Solidi B **248**, 1989 (2011).

nature COMMUNICATIONS

ARTICLE

Received 28 Mar 2015 | Accepted 5 Jun 2015 | Published 16 Jul 2015 DOI: 10.1038/ncomms8766 OPEN

Chemical structure imaging of a single molecule by atomic force microscopy at room temperature

Kota Iwata[1], Shiro Yamazaki[2], Pingo Mutombo[3], Prokop Hapala[3], Martin Ondráček[3], Pavel Jelínek[3,1] & Yoshiaki Sugimoto[1,4]

Atomic force microscopy is capable of resolving the chemical structure of a single molecule on a surface. In previous research, such high resolution has only been obtained at low temperatures. Here we demonstrate that the chemical structure of a single molecule can be clearly revealed even at room temperature. 3,4,9,10-perylene tetracarboxylic dianhydride, which is strongly adsorbed onto a corner-hole site of a Si(111)-(7 × 7) surface in a bridge-like configuration is used for demonstration. Force spectroscopy combined with first-principle calculations clarifies that chemical structures can be resolved independent of tip reactivity. We show that the submolecular contrast over a central part of the molecule is achieved in the repulsive regime due to differences in the attractive van der Waals interaction and the Pauli repulsive interaction between different sites of the molecule.

---

[1] Graduate School of Engineering, Osaka University, 2-1, Yamada-Oka, Suita, Osaka 565-0871, Japan. [2] The Institute of Scientific and Industrial Research, Osaka University, 8-1 Mihogaoka, Ibaraki, Osaka 567-0047, Japan. [3] Institute of Physics, Academy of Sciences of the Czech Republic, Cukrovarnická 10/112, Prague 16200, Czech Republic. [4] Department of Advanced Materials Science, University of Tokyo 5-1-5, Kashiwanoha, Kashiwa, Chiba 277-8561, Japan. Correspondence and requests for materials should be addressed to Y.S. (email: ysugimoto@k.u-tokyo.ac.jp).

Atomic force microscopy (AFM) with a frequency modulation technique[1] has proven successful for imaging various sample surfaces at high resolution[2,3]. Since the first-reported use of AFM to image the chemical structures of single organic molecules[4], numerous molecular studies have employed AFM, such as for the structural determination of natural compounds[5], the imaging of intracharge distributions[6,7], bond order discrimination[8], discrimination of products after chemical reactions[9] and intermolecular contrasts[10–13]. Chemical structures can also be obtained by scanning tunnelling microscopy (STM) using single atoms or molecules below/on the tip as transducers[14,15]. Thus far, such studies have been performed at 5 K, except for a few reports at 77 K (refs 11,16,17). Most investigators have used the so-called qPlus sensor[18], in which one free-standing prong of a quartz tuning fork acts as a stiff cantilever, while the other prong is fixed. The short-range interaction force is selectively detected by small cantilever oscillation amplitude (A). In addition, functionalized tips, such as the CO-terminated tip, are effective in enhancing spatial resolution[19].

In this study, we demonstrate that the chemical structure of single molecules can be revealed by AFM even at room temperature (RT). Such RT imaging is challenging because CO tip functionalization is not feasible, and it is relatively hard to maintain a stable-tip state. RT imaging can be achieved by AFM, however, by using optical interferometry with high force sensitivity and soft silicon cantilevers. Submolecular AFM imaging at RT offers great promise for further application.

Results

High-resolution AFM imaging of a single molecule. The present experiments were performed by using a custom-built AFM/STM operated at RT under an ultrahigh vacuum[20]. Commercial conductive Si cantilevers were used after Ar ion sputtering treatment. The cantilever was oscillated at relatively large amplitude ($A \sim 10$ nm) for stable operation. A sharp Si tip is essential to maintain stable-tip states at RT, and to suppress long-range interaction force contributions[21]. The cantilever deflection was detected by an optical interferometer with high sensitivity[22]. The frequency shift (Δf) of the cantilever oscillation was recorded as an AFM signal. The time-averaged tunnelling current was measured from the cantilever while bias voltage (V_S) was applied to a sample. V_S was set to compensate contact potential difference ($V_{\mathrm{c.p.d.}}$) for AFM. We investigated PTCDA (3,4,9,10-perylene tetracarboxylic dianhydride) molecules evaporated on a reactive semiconductor surface, that is, the Si(111)-(7 × 7) surface.

We first used STM to investigate the very initial adsorption of PTCDA molecules onto the Si(111)-(7 × 7) surface. Some PTCDA molecules were adsorbed onto corner-hole sites in a well-defined manner, as first reported by Nicoara *et al.*[23]. A typical STM topographic image is shown in Fig. 1a. Characteristic features appear on the molecule in the centre of the image beside the atomic resolution of the Si(111)-(7 × 7) surface. Figure 1b shows the proposed adsorption geometry corresponding to the topographic image in Fig. 1a. The aromatic rings at the centre of the molecule are well detached from the Si substrate, since atoms are missing up to the third layer at the corner-hole sites. In contrast, the carboxyl groups of the molecule strongly bind with dangling bonds of the four corner Si adatoms by partial ionic covalent bonding[23]. The bonds are strong enough to suppress thermal diffusion of the molecule even at RT. In our empty-state STM image, five parallel stripes are imaged in the molecule as indicated by the arrows in Fig. 1a. They were identified as originating from a molecular orbital that was located near the Fermi level and was energetically shifted from the original LUMO + 1 and LUMO + 2 because of molecule–substrate coupling[23].

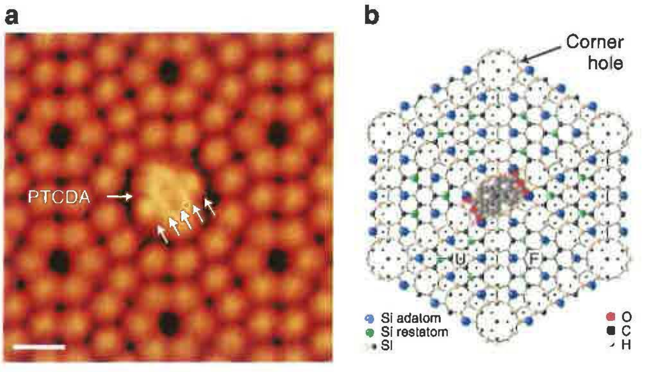

Figure 1 | A single PTCDA molecule adsorbed on the Si(111)-(7 × 7) surface. (**a**) An STM image at $V_s = +500$ mV. Scale bar, 1 nm. The five arrows indicate stripes corresponding to a molecular orbital. (**b**) Schematic view of the arrangement of a PTCDA molecule adsorbed onto the surface over a corner-hole site.

When a PTCDA molecule was found at a corner-hole site by STM, we switched the imaging mode to a constant-height AFM scan[21]. The tip–surface distances were gradually decreased until the repulsive force became significant on the molecule. In some cases, the contrast was unclear or the tip state changed or the molecule moved away from the original location by the tip before the tip reached the distance for submolecular resolution as shown in Supplementary Fig. 1. Then, the tip was modified by intentionally crashing it into the clean region of the Si surface to obtain stable tips. We then tried again to image the molecule. By repeating these procedures, we successfully obtained AFM images of single molecules, revealing their chemical structure even at RT, as shown in Fig. 2a. Five centre-carbon rings were clearly resolved by the local positive shift of Δf due to the Pauli repulsive force. Thus, AFM and STM clearly offer complementary information, that is, chemical structure and molecular orbital data, respectively. The detailed procedures for high-resolution AFM imaging are described in Methods and Supplementary Fig. 1.

To gain insight into the geometry of the molecule and imaging mechanism, we carried out density functional theory (DFT) calculations. The top and side views of the optimized configuration of the molecule adsorbed on the Si(111)-(7 × 7) surface are shown in Fig. 2c,d, respectively. Oxygen atoms were located above Si adatoms by 1.6 Å. Furthermore, the molecule was bent upward by 1.0 Å. This may have been due to the directionality of the Si-dangling bonds that are bound with the oxygen atoms. The central part of the molecule thus protruded from the Si adatoms by 2.6 Å.

The bend of the molecule explains the invisibility of the carboxyl parts in PTCDA at constant-height scan, as shown in Fig. 2a. Only the more protruding central part of the molecule is imaged. Our Δf image could be reproduced by a calculated map of electron density cut along a plane parallel to the Si(111)-(7 × 7) surface (see Fig. 2b). Electron density was high mainly at the five carbon rings at a constant-height. In previous theoretical calculations using the same molecule[24], features in the electron density map were in good agreement with those in the Δf map, as well as with the map of kinetic energy. The enhancement of kinetic energy as the tip approaches shows the origin of the Pauli repulsive force.

Tip characterization by force measurements and calculation. We were able to obtain the chemical structure using Si cantilevers. Although CO tip functionalization is not currently possible

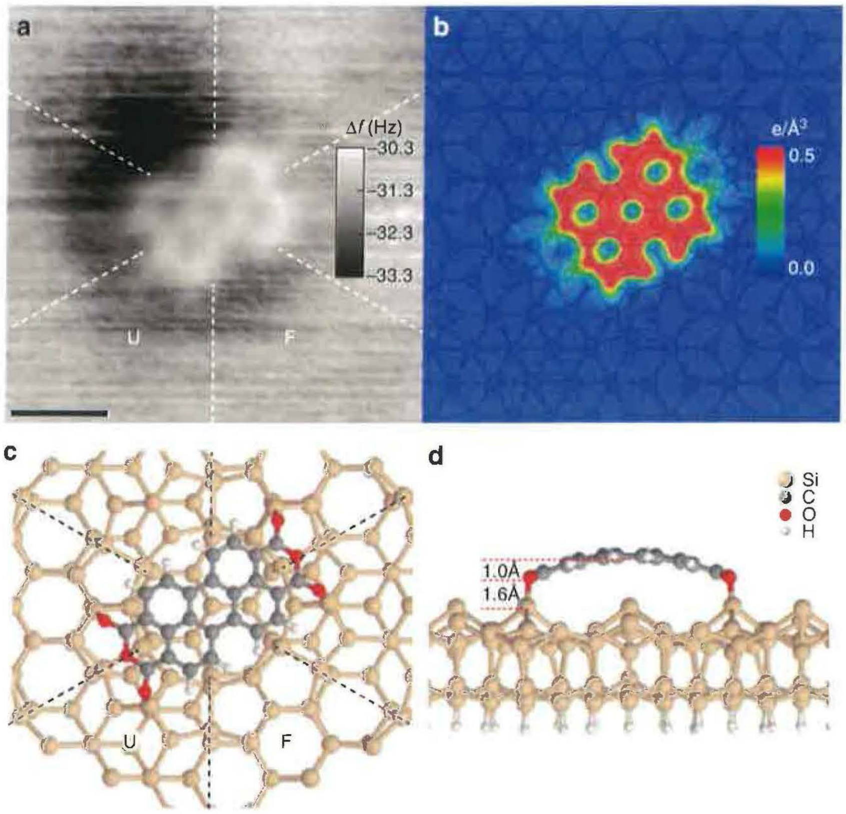

Figure 2 | Chemical structure imaging of single molecule by AFM at room temperature. (**a**) Constant-height AFM image of a single PTCDA molecule adsorbed on the Si(111)-(7 × 7) surface. The acquisition parameters were $f_0 = 158{,}586.6$ Hz, $k = 31.9$ N/m, $A = 138$ Å, $V_s = V_{\mathrm{c.p.d.}} = 130$ mV, and $Q = 22{,}000$. The scan speed was 3 nm s^{-1}. Scale bar, 0.5 nm. (**b**) Calculated map of electron density cut along a plane parallel to the surface. (**c**,**d**) Top and side views of the optimized configuration of the PTCDA molecule adsorbed at a corner-hole site of the Si(111)-(7 × 7) surface.

at RT, we can characterize the tip state that would be capable of producing chemical structures in the molecule by force measurements. For this purpose, we carried out force spectroscopy using the same tip at three different sites, that is, the centre of the molecule, a corner Si adatom sufficiently far from the molecule, and a bare corner hole. The distance dependences of Δf curves with two different types of tips are shown in Fig. 3a,b. $\Delta f(z)$ curves on the corner hole (gray curves), which corresponded to the long-range force, were fitted into an inverse power function. The fitting curves were subtracted from the $\Delta f(z)$ curves above the molecules (blue curves) and the Si adatoms (red curves). The obtained short-range part of the $\Delta f(z)$ curves was converted into the short-range forces ($F(z)$) using the conversion formula[25] (see the solid blue and red curves in Fig. 3c,d). Similar to our previously reported study[26], the tips in Fig. 3c,d could be classified as a reactive tip and non-reactive tip, respectively. They were characterized by the magnitude of the maximum attractive force on the Si adatoms. Reactive tips produce a strong chemical bonding force (>0.5 nN) on an Si adatom site, while non-reactive tips produce a weak physical force (<0.1 nN). This is partly because reactive tips have dangling bonds that hybridize with the dangling bonds on Si adatoms to form covalent bonds. Non-reactive tips do not have dangling bonds, that is, they are chemically inert. Clear atomic resolution of each Si adatom on the Si(111)-(7 × 7) surface can be obtained only with reactive tips. Nevertheless, we found that both types of tips could produce an image of the inner molecular structure by Pauli repulsion, as shown in the insets of Fig. 3a,b. This is also evident from the similarity of the $F(z)$ curves on the molecule with the different types of tips (see the blue curves in Fig. 3c,d). In both types of tips, weak maximum attractive forces (approximately -0.27 nN) are obtained on the molecule before the tips enter the repulsive-force region ($F>0$).

This result was comparable to our previous findings on H-terminated Si adatoms on the Si(111)-(7 × 7) surface[26]. AFM images showed contrast corresponding to the repulsive force on H atoms with both types of tips[26]. For comparison, both types of $F(z)$ curves previously measured on H-terminated Si adatoms are shown in Fig. 3c,d (green dotted curves). $F(z)$ curves on Si adatoms measured by the same tips are also shown (orange dotted curves); these curves were duplicated from Fig. 6a,b in our previous paper[26]. The curves on Si adatoms in the present studies are in good correspondence with the previous ones, implying that the tip states are very similar (that is, the Si(001) dimer tip for Fig. 3c and OH-terminated dimer tip for Fig. 3d, as previously identified by DFT calculation). The formation of the OH-terminated tip originates from the residual H_2O gas inside the ultrahigh vacuum chamber. The tip models are shown in the insets of Fig. 3c,d. The $F(z)$ curves on the H sites measured by these reactive and non-reactive tips are similar. The maximum attractive forces on the H sites are tiny (<0.1 nN) for both types of tips. They are smaller than those on the PTCDA molecules, where the carbon atoms composing the centre rings contribute to the physical force.

The termination of the non-reactive tip by the -OH group can also explain the enhanced submolecular resolution of the AFM image shown on Fig. 3b, in comparison with the reactive counterpart shown in Fig. 3a. This effect can be attributed to the much smaller atomic radius of the frontier H atom in the case of -OH group in comparison with the apex Si atom on the reactive

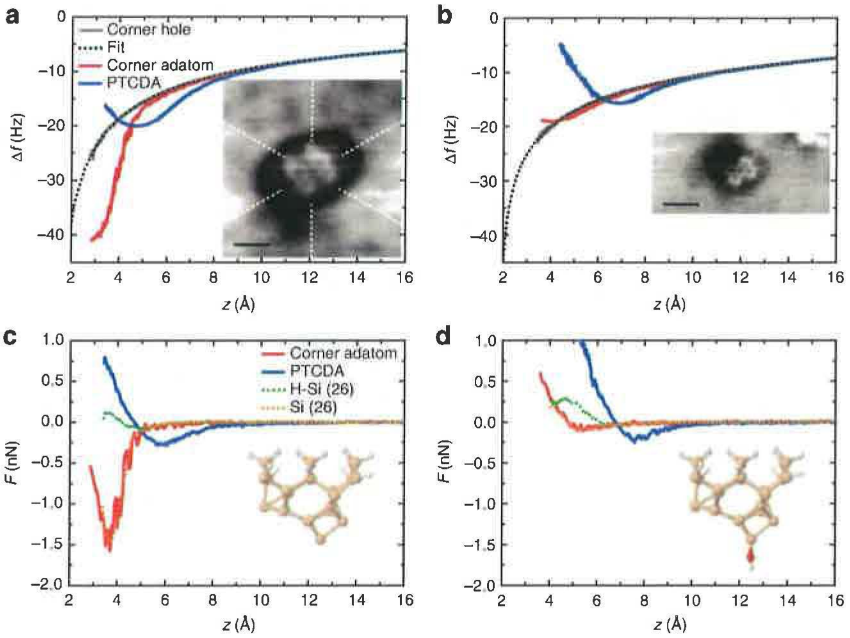

Figure 3 | Tip identification by force measurements. **(a,b)** $\Delta f(z)$ curves measured over the centre of the PTCDA molecules (blue), corner adatoms (red) and corner holes (gray) using **(a)** a reactive tip and **(b)** an inert tip. Fitting curves for the long-range force contributions are shown by the dotted curves. The acquisition parameters were **(a)** $f_0 = 165{,}371.4$ Hz, $k = 37.6\,\mathrm{N\,m^{-1}}$, $A = 133$ Å, $V_s = V_{\mathrm{c.p.d.}} = -280$ mV and $Q = 23{,}000$, **(b)** $f_0 = 156{,}719.7$ Hz, $k = 29.6\,\mathrm{N\,m^{-1}}$, $A = 201$ Å, $V_s = V_{\mathrm{c.p.d.}} = -350$ mV and $Q = 25{,}000$. Corresponding AFM images are shown in the insets. Scale bar, 1 nm. **(c,d)** $F(z)$ curves over the centre of the PTCDA molecules (blue) and corner adatoms (red), converted from the short-range part of the $\Delta F(z)$ curves from **a** and **b**. The $F(z)$curves over the H adsorbed on Si adatoms (green) and Si adatoms (orange) from our previous study[26] are also shown. The tip models identified are shown in the insets.

tip. The smaller apex atom can penetrate deeper into the interatomic voids (that is, benzene rings), providing higher submolecular contrast as was discussed in ref. 12.

We conclude that tip reactivity is not crucial for chemical structure imaging when the tip scans on the inert closed-shell molecule that is strongly bound on the semiconductor surface. We calculated $F(z)$ on some points of the PTCDA molecule using the Si dimer tip model as described below. The maximal attractive force was small over all sites, including an edge oxygen atom bonded to an Si adatom, since the reactive orbital of the oxygen atom was terminated by the surface Si adatom. The molecule can be stably imaged even using a reactive tip. Our results are also consistent with a recent study of NTCDI molecules on the Si(111)-(7 × 7) surface at low temperature[11,27].

Next, we used force spectroscopic data to further clarify the difference in tip height required for atomic resolution between the molecule and Si surface. In Fig. 2a, high resolution was obtained only on the molecule, while there was no atomic resolution on the Si(111)-(7 × 7) surface. In our $F(z)$ curves acquired using a number of tips with both types of reactivity, the difference in the distances for maximum attractive force between molecules and Si adatoms was about 2 Å (see Fig. 3c,d). This can be explained by the topographic height difference between the molecule and Si adatom layer as seen in Fig. 2d. When the tip–sample distance for constant-height imaging was gradually decreased, the tip started to interact with the molecule first. At the repulsive region ($F > 0$) on the molecule in Fig. 3c, the reactive tip reached the onset of the short-range force on Si adatoms. There, atomic resolution on Si adatoms could be obtained by attractive force contrast, as shown in the inset of Fig. 3a. On the other hand, the non-reactive tips could not provide clear atomic resolution on the Si adatoms by attractive force. It may have been expected that both types of tips would be capable of providing atomic resolution on Si adatom sites by repulsive interaction forces at very close distances, since such resolution was indeed recently obtained at low temperature[16]. However, we found that it was difficult to scan at such close distances at RT without tip changes.

Discussion

Theoretical short-range force $F(z)$ curves on the centre of the molecule and Si adatoms are plotted in Fig. 4a. The corresponding experimental curves from Fig. 3c are also shown. As mentioned above, the Si dimer tip reproduced the experimental $F(z)$ curve measured above the Si adatom (see the red and orange curves). In addition, the $F(z)$ curve calculated on the molecule well reproduced the features of the experimental curve, such as the maximum attractive force (see the blue and light blue curves).

To gain more insight into the mechanism of the submolecular contrast, we analysed the differences among the short-range force $F(z)$ curves calculated for three characteristic sites of the PTCDA molecule, that is, an oxygen (O), a hollow (h) and a carbon (C) site (see Fig. 4c). The calculated $F(z)$ curves are shown in Fig. 4b. According to our DFT simulations, the van der Waals (vdW) interaction represented most of the attractive portion of the $F(z)$ curves in far tip-sample distances. The vdW interaction provides a common attractive background with a larger maximum on the h-site than on the C-site. The characteristic bending of the molecule causes the largest attractive interaction over the O-site, which is shifted downward with respect to the central part of the molecule. At close distances, the Pauli repulsion between electronic clouds on the tip and sample prevails, and it is larger at the areas of higher electron density (for example, on top of the carbon atoms; see Fig. 2b). The presence of the Pauli repulsion further enhances the difference between the short-range forces $F(z)$ calculated at the three characteristic sites. This effect is responsible for the observed submolecular contrast.

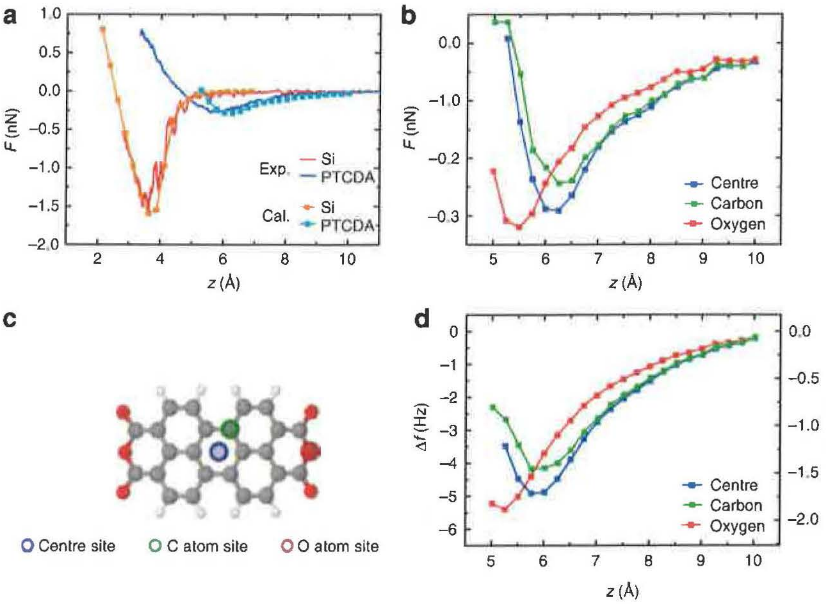

Figure 4 | Theoretical force and frequency shift curves. (**a**) Theoretical $F(z)$ curves over the centre of a PTCDA (light blue) and a corner adatom (orange). The model of an Si dimer tip shown in Fig. 3c is used. The corresponding experimental curves from Fig. 3c are shown: $F(z)$ on PTCDA (blue) and Si adatom (red). The Van der Waals (vdW) force is taken into account for the calculations on the molecule. The theoretically derived maximum attractive force is around -0.29 nN, which matches the value obtained experimentally. Since the attractive force in the $F(z)$ calculated without the vdW contribution is too small to reproduce the experimental results (not shown), the vdW interaction force dominates the attractive force on the molecule. (**b**) Theoretical $F(z)$ curves over the centre of a PTCDA (blue), a carbon atom (green) and an oxygen atom (red). (**c**) A model of the PTCDA molecule showing the three sites used for the force calculations. (**d**) $\Delta f(z)$ curves converted from the $F(z)$ curves shown in **b**. For the conversion, we used the same parameters as used for the experiments shown in Fig. 3a.

Next, we estimated the tip-sample distance, where the submolecular image was acquired. For this purpose, we compared the change of the normalized frequency shift γ[28] among the three characteristic O, h and C sites between experiment and theory. From the high-resolution experimental image obtained with a reactive tip (inset of Fig. 3a), we could estimate that the γ values were -4.7, -4.5 and -5.25 [fN$\cdot$m$^{1/2}$] for the h, C and O-site, respectively. Thus we obtain following differences $\gamma_{h\text{-}O}=\gamma_h-\gamma_O=+0.55$ [fN$\cdot$m$^{1/2}$] and $\gamma_{h\text{-}C}=-0.2$ [fN$\cdot$m$^{1/2}$], respectively. These differential values were well reproduced in the theoretical curves $\gamma_{h\text{-}O}=+0.7$ and $\gamma_{h\text{-}C}=-0.3$ [fN$\cdot$m$^{1/2}$] at distance $z=5.25$ Å (see Fig. 4d). Therefore, we can conclude that the submolecular contrast over the central part of the molecule was achieved in the repulsive regime due to the difference in the attractive vdW and, Pauli repulsive interactions, with the latter making the major contribution.

Note that both the submolecular images acquired with the reactive and those acquired with the non-reactive Si-based tips show relatively blunt contrast, which matches the submolecular contrast observed on the PTCDA/Ag(111) surface in relatively far distances (see Fig. 2c in ref. 12). In the distance range, the distortion of a functionalized probe does not play any role and the contrast is completely driven by the difference in the force over different sites (hollow, atom). This concurs very well with the fact that we are able to achieve the submolecular contrast even with a relatively rigid, bare Si-tip. This leads to an important question, namely, can a sharp submolecular resolution be realized using Si-based tips with an intentionally functionalized group at RT? In principle, such resolution could be hampered by two factors: (i) the presence of inherent noise due to thermal fluctuation, and/or; (ii) the instability of a functional group on the tip apex. Thus the further improvement of the submolecular resolution is open to question. We believe that this question will be addressed in the near future.

In conclusion, we successfully obtained the chemical structure of single PTCDA molecules (1) on a semiconducting Si surface; (2) at room temperature; (3) using soft Si cantilevers; and (4) under oscillation at large amplitude. Force spectroscopic measurements showed that high resolution could be obtained independently of the tip reactivity. The DFT calculations clarified the geometry of the molecule and the origin of the high-resolution AFM image reflecting the electron density map over the molecule. Our less-restrictive method for submolecular imaging opens a new route for further applications using AFM. We believe that this work will stimulate an effort to achieve chemical structure imaging of single molecules even in ambient and liquid environments using high-resolution AFM based on Si cantilevers[29,30].

Methods

Procedures for high-resolution molecular imaging by AFM. We obtained high-resolution molecular AFM images according to the following protocol. (1) Search for PTCDA molecules that are adsorbed at the corner-hole sites by STM under a dynamic mode. (2) Switch from the operation mode to the AFM topographic mode. Set the tip–surface distance to be large so that AFM will not have atomic/molecular resolution. (3) Start the constant-height scan in the retrace mode, in which each fast-scan line is scanned twice[31]. Close the distance feedback loop in the first scan and open it in the second scan. In the first scan, the tip–surface distance will be large and thus the obtained atomic-scale contrast will not have surface features. Perform the second scan along a line parallel to the linear fitting of the first scan while recording Δf. The tip–surface distance can be controlled by offset from the first scan height. (4) Gradually increase the offset to reduce the tip–surface distance for the second constant-height scan until submolecular resolution is obtained on the molecules. The tip states will change or the contrast will not be clear or the molecule will be moved at very small tip–surface distances at RT. Then, modify the tip state using the following procedures. (i) Scan the surface by dynamic STM. To modify the tip, gently poke it into the surface by controlled force distance spectroscopy, reaching the strong repulsive regime[32]. Bring the tip to the clean Si region and open the distance feedback. Then, allow the tip to approach the surface by a certain displacement while recording the tunnelling current and Δf. If no abrupt jump is observed in either channel, then repeat the procedure with increasing displacement until an abrupt change of signals is observed in accompaniment with the tip change. (ii) Next, rescan the surface by dynamic STM to check the tip quality. If the tip is unstable or shows multi-tip features, then high-resolution molecular imaging cannot be achieved by AFM. Then, we again modify the tip by returning to step (i). (iii) When the tip is optimized in STM, restart the molecular imaging procedure at step (1) above. AFM images, which were obtained before Fig. 2a and Fig. 3a were acquired, are shown in Supplementary Fig. 1.

Consideration of the signal-to-noise ratio for AFM imaging. Chemical structures can be successfully obtained at RT using Si cantilevers oscillated even at large A. To achieve such high resolution, tiny force differences reflecting electron density should be detected through the AFM observable, which is Δf. A signal-to-noise ratio (S/N) in Δf for constant-height AFM imaging has been previously discussed[21]. Here we show that a soft Si cantilever with an optical interferometer has a higher S/N than the qPlus sensor popularly used. The Δf signal is proportional to f_0/k, where f_0 and k are the resonance frequency and stiffness of a cantilever, respectively. This factor in our Si cantilever ($f_0 = 160\,\mathrm{kHz}$, $k = 30\,\mathrm{N/m}$) is 400 times larger than that in a typical quartz cantilever ($f_0 = 23\,\mathrm{kHz}$, $k = 1{,}800\,\mathrm{N/m}$). In addition, the Δf signal increases with decreasing A. Δf is proportional to $1/A^{1.5}$ at large A approximation[33]. Since a soft Si cantilever should be oscillated at large A to avoid instability, an Si cantilever has a smaller signal than a quartz cantilever. This factor for an Si cantilever oscillated at $A = 20\,\mathrm{nm}$ becomes at most 2,800 times smaller than that of a quartz cantilever oscillated at $A = 0.1\,\mathrm{nm}$. On the other hand, the deflection noise in Δf becomes proportional to n/A, where n is the noise density of the defection sensor[2]. Our optical interferometer has a much smaller n ($15\,\mathrm{fm}/\sqrt{Hz}$)[22] than the typical qPlus sensor ($60\,\mathrm{fm}/\sqrt{Hz}$) at RT[34]. The noise in the Si cantilever with an optical interferometer is 800 times smaller than that in a qPlus sensor. In short, the Si cantilever with an optical interferometer has a better S/N than the qPlus sensor by two orders of magnitude. A large S/N in Δf is essential for constant-height AFM imaging at RT because the scan speed must be fast enough under non-negligible thermal drift.

Calculation method. The simulated $F(z)$ curves with the clean Si dimer tip and the OH-terminated dimer tip were calculated using VASP (Vienna Ab initio Simulation Package)[35]. VASP is a density functional theoretical code that implements a pseudopotential plane wave method. We used Vanderbilt ultrasoft pseudopotentials[36]. The softer version of the oxygen pseudopotentials supplied with VASP was used. The exchange-correlation function was described within the PW91-generalized gradient approximation[37]. We used the semiempirical approach by Grimme[38] for the vdW calculations. The Si(111) surface was represented by a slab consisting of the adatom layer and two more 7×7 Si(111) bi-layers below. The bottom Si atomic layer was passivated with hydrogen atoms. When geometry optimization was performed, the atoms of the PTCDA molecule and 24 Si atoms close to the O–Si bonds were allowed to relax, while all other Si atoms and the saturating hydrogens were kept at fixed positions. We used well-tested Si-based tips[39], where 15 Si atoms at the base of the tip and saturating hydrogen atoms were kept fixed during relaxation. The geometry optimization was converged down to a precision of $10^{-5}\,\mathrm{meV}$ in total energy. The Brillouin zone sampling was restricted to the central (Γ) point. The basis set cutoff for wave function expansion was set to 286.7 eV of kinetic energy, which is the recommended value for carbon pseudopotential (the hardest pseudopotential of the elements used). The maximal wave vector for charge density and local (Hartree) potential expansion was set to twice the maximal wave vector for the wave function expansion (to avoid aliasing effects).

References

1. Albrecht, T. R., Grütter, P., Horne, D. & Rugar, D. Frequency modulation detection using high-Q cantilevers for enhanced force microscope sensitivity. *J. Appl. Phys.* **69,** 668–673 (1991).
2. Giessibl, F. J. Advances in atomic force microscopy. *Rev. Mod. Phys.* **75,** 949–983 (2003).
3. Morita, S., Giessibl, F. J. & Wiesendanger, R. (eds) *Noncontact Atomic Force Microscopy vol.2* (Springer-Verlag, 2009).
4. Gross, L., Mohn, F., Moll, N., Liljeroth, P. & Meyer, G. The chemical structure of a molecule resolved by atomic force microscopy. *Science* **325,** 1110–1114 (2009).
5. Gross, L. *et al.* Organic structure determination using atomic resolution scanning probe microscopy. *Nat. Chem.* **2,** 821 (2010).
6. Mohn, F., Gross, L., Moll, N. & Meyer, G. Imaging the charge distribution within a single molecule. *Nat. Nanotechnol.* **7,** 227–231 (2012).
7. Kawai, S. *et al.* Obtaining detailed structural information about supramolecular systems on surfaces by combining high-resolution force microscopy with ab initio calculations. *ACS Nano* **10,** 9098 (2013).
8. Gross, L. *et al.* Bond-order discrimination by atomic force microscopy. *Science* **337,** 1326–1329 (2012).
9. deOteyza, D. G. *et al.* Direct imaging of covalent bond structure in single-molecule chemical reactions. *Science* **340,** 1434–1437 (2013).
10. Zhang, J. *et al.* Real-space identification of intermolecular bonding with atomic force microscopy. *Science* **342,** 611–614 (2013).
11. Sweetman, A. M. *et al.* Mapping the force field of a hydrogen-bonded assembly. *Nat. Commun.* **5,** 3931 (2014).
12. Hapala, P. *et al.* Mechanism of high-resolution STM/AFM imaging with functionalized tips. *Phys. Rev. B* **90,** 085421 (2014).
13. Hamalainen, S. *et al.* Intermolecular contrast in atomic force microscopy images without intermolecular bonds. *Phys. Rev. Lett.* **113,** 186102 (2014).
14. Weiss, C., Wagner, C., Temirov, R. & Tautz, F. Direct imaging of intermolecular bonds in scanning tunneling microscopy. *J. Am. Chem. Soc.* **132,** 11864–11865 (2010).
15. Chiang, C.-L., Xu, C., Han, Z. & Ho, W. Real-space imaging of molecular structure and chemical bonding by single-molecule inelastic tunneling probe. *Science* **344,** 885–888 (2014).
16. Sweetman, A. *et al.* Intramolecular bonds resolved on a semiconductor surface. *Phys. Rev. B* **90,** 165425 (2014).
17. Moreno, C., Stetsovych, O., Shimizu, T. & Custance, O. Imaging three-dimensional surface objects with submolecular. *Nano Lett.* **15,** 2257 (2015).
18. Giessibl, F. J. Atomic resolution on Si(111)-(7x7) by noncontact atomic force microscopy with a force sensor based on a quartz tuning fork. *Appl. Phys. Lett.* **76,** 1470–1472 (2000).
19. Gross, L. Recent advances in submolecular resolution with scanning probe microscopy. *Nat. Chem.* **3,** 273–278 (2011).
20. Sugimoto, Y. *et al.* Quantum degeneracy in atomic point contacts revealed by chemical force and conductance. *Phys. Rev. Lett.* **111,** 106803 (2013).
21. Sugimoto, Y. *et al.* Simultaneous AFM and STM measurements on the Si(111)-(7x7) surface. *Phys. Rev. B* **81,** 245322 (2010).
22. Morita, K., Sugimoto, Y., Sasagawa, Y., Abe, M. & Morita, S. Small-amplitude dynamic force microscopy using a quartz cantilever with an optical interferometer. *Nanotechnology* **21,** 305704 (2010).
23. Nicoara, N. *et al.* Adsorption and electronic properties of ptcda molecules on Si(111)-(7x7): Scanning tunneling microscopy and first-principles calculations. *Phys. Rev. B* **82,** 075402 (2010).
24. Moll, N., Gross, L., Mohn, F., Curioni, A. & Meyer, G. A simple model of molecular imaging with noncontact atomic force microscopy. *N. J. Phys.* **14,** 083023 (2012).
25. Sader, J. E. & Jarvis, S. P. Accurate formulas for interaction force and energy in frequency modulation force spectroscopy. *Appl. Phys. Lett.* **84,** 1801–1803 (2004).
26. Yurtsever, A. *et al.* Force mapping on a partially h-covered Si(111)-(7x7) surface: Influence of tip and surface reactivity. *Phys. Rev. B* **87,** 155403 (2013).
27. Sang, H. *et al.* Identifying tips for intramolecular NC-AFM imaging via in situ fingerprinting. *Sci. Report* **4,** 6678 (2014).
28. Giessibl, F. J. Forces and frequency shifts in atomic-resolution dynamic-force microscopy. *Phys. Rev. B* **56,** 16010–16015 (1997).
29. Fukuma, T., Ueda, Y., Yoshioka, S. & Asakawa, H. Atomic-scale distribution of water molecules at the mica-water interface visualized by three-dimensional scanning force microscopy. *Phys. Rev. Lett.* **104,** 016101 (2010).
30. Ido, S. *et al.* Immunoactive two-dimensional self-assembly of monoclonal antibodies in aqueous solution revealed by atomic force microscopy. *Nat. Mater.* **13,** 264–270 (2014).
31. Yurtsever, A., Sugimoto, Y., Fukumoto, M., Abe, M. & Morita, S. Effect of tip polarity on Kelvin probe force microscopy images of thin insulator CaF2 films on Si(111). *Appl. Phys. Lett.* **101,** 083119 (2012).
32. Sugimoto, Y. *et al.* Complex patterning by vertical interchange atom manipulation using atomic force microscopy. *Science* **322,** 413–417 (2008).
33. Giessibl, F. J. & Bielefeldt, H. Physical interpretation of frequency-modulation atomic force microscopy. *Phys. Rev. B* **61,** 9968–9971 (2000).
34. Giessibl, F., Pielmeier, F., Eguchi, T., An, T. & Hasegawa, Y. Comparison of force sensors for atomic force microscopy based on quartz tuning forks and length-extensional resonators. *Phys. Rev. B* **84,** 125409 (2011).
35. Kresse, G. & Furthmüller, J. Efficient iterative schemes for ab initio total-energy calculations using a plane-wave basis set. *Phys. Rev. B* **54,** 11169–11186 (1996).
36. Vanderbilt, D. Soft self-consistent pseudopotentials in a generalized eigenvalue formalism. *Phys. Rev. B* **41,** 7892–7895 (1990).
37. Perdew, J. *et al.* Atoms, molecules, solids, and surfaces: Applications of the generalized gradient approximation for exchange and correlation. *Phys. Rev. B* **46,** 6671–6687 (1992).
38. Grimme, S. Accurate description of van der Waals complexes by density functional theory including empirical corrections. *J. Comput. Chem.* **25,** 1463–1473 (2004).
39. Pou, P. *et al.* Structure and stability of semiconductor tip apexes for atomic force microscopy. *Nanotechnology* **20,** 264015 (2009).

Acknowledgements

This work was supported by a Grant-in-Aid for Scientific Research (265691, 15H03566, 26600015, 26110516, 2603355) from the Ministry of Education, Culture, Sports, Science and Technology of Japan, by the Funding Program for Next Generation World-Leading Researchers, and through the financial support of GACR 14-16963J.

Author contributions

Y.S. conceived and designed the experiments; K.I performed the experiments; P.M, M.O, P.H. and P.J. performed the theoretical analysis; Y.S. and P.J. wrote the paper. All authors analysed the data, discussed the results and commented on the manuscript.

Additional information

Supplementary Information accompanies this paper at http://www.nature.com/naturecommunications

Competing financial interests: The authors declare no competing financial interests.

Reprints and permission information is available online at http://npg.nature.com/reprintsandpermissions/

How to cite this article: Iwata, K. *et al.* Chemical structure imaging of a single molecule by atomic force microscopy at room temperature. *Nat. Commun.* 6:7766 doi: 10.1038/ncomms8776 (2015).